AIChE

Multiphase Flow and Mixing in Dilute Bubble Swarms

Stefan Radl
Institute for Process and Particle Engineering, Graz University of Technology, A-8010 Graz, Austria

Johannes G. Khinast
Institute for Process and Particle Engineering and Research Center Pharmaceutical Engineering GmbH, Graz University of Technology, Inffeldgasse 21a/II, A-8010 Graz, Austria

DOI 10.1002/aic.12154
Published online January 27, 2010 in Wiley Online Library (wileyonlinelibrary.com).

High-fidelity three-dimensional (3-D) simulations of multiphase flow and mixing in dilute bubble swarms were performed using the Euler-Lagrange simulation approach. Included was species transport, as well as complex chemical reactions in the simulations. It was found that the algebraic SGS model satisfactory predicts experimental data for the mean flow field. A detailed description of multiphase flow was used and developed to simulate the time evolution of scalar and reactive mixing in a bubble column. An analysis involving the scale of segregation Φ, a metric that characterizes the mean driving force for mixing, is applied for the first time to multiphase flow. The study shows that Φ is inversely proportional to the bubble diameter at constant gas-feed rate, but only a weak function of the gas-feed rate. Also, we observed significant differences of mixing metrics in reactive and nonreactive systems. © 2010 American Institute of Chemical Engineers *AIChE J,* 56: 2421–2445, 2010
Keywords: bubble columns, multiphase flow, mass transfer, bioreactors, large eddy simulation

Introduction

Reactive multiphase flows can be found in many applications in the chemical, pharmaceutical and biotechnology industries. Typical examples include the Fischer-Tropsch synthesis,[1] catalytic hydrogenations,[2] oxidations,[3] the production of benzoic acid[4] or the aeration of bioreactors, e.g., for the production of penicillin or EPO.[5] However, a detailed mathematical description of these flows is still challenging, since the interaction of mixing, mass transfer and the (bio-) chemical reactions dominates the yield, selectivity or productivity of the reactor, which complicates the design and optimization of such processes. For example, certain cell cultures are highly shear-sensitive and vigorous agitation, while improving mass transfer and mixing, maybe reduce productivity and product quality due to shear-related necrotic and apoptotic effects or due to damage of the target protein. Another well-known example for mixing-sensitive reaction systems of industrial interest are catalytic oxidations using pure oxygen.

In order to study reactive multiphase flows in detail, experimental and numerical methods have been used in the past. State-of-the-art experimental tools include the use of laser optical methods (laser-Doppler-anemometry, LDA; as well as phase-Doppler-anemometry, PDA) for bubbles up to 1 mm in dia., as well as tomographic methods and particle image velocimetry (PIV) for systems involving larger bubbles. Using the latter technique it is possible to determine the velocity fields of both phases and to measure the shape and size of individual bubbles using specialized illumination techniques.[6] Such methods are crucial for the model validation of bubbly flows and have encouraged many groups to perform highly detailed numerical simulations of these flows. Also, concentration fields around single bubbles have been

Correspondence concerning this article should be addressed to J. G. Khinast at khinast@TUGraz.at.

© 2010 American Institute of Chemical Engineers

measured using the laser-induced fluorescence technique (LIF).[7–10] In these methods, a laser sheet is used to record the instantaneous concentration fields of a dissolving, nonreacting species in the liquid phase. For example, Bork et al.[7] have combined LIF with PIV to develop a novel mass-transfer correlation for bubbles with wake shedding. However, all of these studies concentrate on the dissolution of an inert scalar and a direct experimental quantification of chemical reactions in the vicinity of gas-liquid interfaces of bubbly flows has not been reported. The same is true for the direct quantification of scalar mixing within bubble swarms. Experimental studies in literature involve either very simple qualitative experiments using ink (see, e.g., Wiemann[11]) or more quantitative techniques, using radioactive particles (see, e.g., Yang et al.[12]), liquid phases with different temperatures (see, e.g., Lorenz et al.[13]), or colored solutions together with photometers (see, e.g., Yang et al.[14]). When using these quantitative techniques it is not possible to measure the instantaneous concentration of a tracer substance in the whole flow field, but only at distinct locations. Consequently, scalar mixing can be quantified only by integral parameters, e.g., an axial dispersion coefficient. To the best of our knowledge, the details of (spatially resolved) scalar mixing in a bubble column have not been the focus of experimental studies so far. For the Becker case studied in this work, not even experimental data for scalar mixing in terms of integral parameters (e.g., dispersion coefficients) exist.

For the computational analysis of bubbly flows different methods have been developed, each of them having different advantages and drawbacks. An overview over the currently available approaches and future challenges can be found in Sundaresan,[15] as well as in Koynov and Khinast.[16] Also, Sommerfeld and Decker[17] provide a detailed overview of the subject with a focus on stirred tanks.

In analogy to single-phase simulations, a variety of methods can be used to describe turbulent flows in multiphase reactors, including (a) a full resolution of all scales with direct numerical simulations (DNS), (b) the use of a filtered set of the momentum equations via so-called large eddy simulations (LES), and (c) the use of the ensemble-averaged Navier-Stokes equations, either steady or unsteady, often referred to as the Reynolds-averaged-Navier-Stokes (RANS) approach.

Currently, the most detailed methods allow the analysis of the deformation of individual bubbles, which are here referred to as multiphase direct numerical simulations (MDNS), because they usually involve DNS of all the phases. These techniques include the volume of fluid method (e.g., the recent work by Kim and Lee[18]), Lagrangian methods (where the grid follows the gas-liquid interface, e.g., Li et al.[19] and Hameed et al.[20]), as well as the front-tracking (FT) method introduced by Unverdi and Tryggvason.[21] The latter method has attracted numerous groups[22–29] to study also mixing effects including chemical reactions. For example Koynov, Khinast and Tryggvason[22] used the FT method for the first time to study reactive bubble swarms ($\sim$100 bubbles) with fully-resolved deformable and dynamic interfaces.[22] Earlier work by our group also included heterogeneously catalyzed reactions close to bubbles.[30]

Another approach is the Euler-Euler (EE) method, which treats the involved phases as interpenetrating continua. The advantage of this method is that the number of particles is not limiting, as there are no particles or bubbles. Hence, the simulation of large-scale reactors becomes feasible. However, the interface between the phases is not resolved, and, consequently, sophisticated closure models that predict the local bubble size have to be used to correctly describe the interaction of the involved phases. Often, a population balance equation (PBE) needs to be solved in conjunction with mass, momentum and possibly the energy balance, which is computationally demanding. In addition it can cause instabilities in the solution procedure and is still a topic of active research, as breakage and coalescence kernels cannot be predicted from theory alone and remain somewhat of a fitting parameter.[1,31]

The last major approach is the Lagrangian particle tracking (LPT) method in which the disperse phase, e.g., the individual bubbles, are tracked in the flow field as point sources. The motion of the continuous phase is solved on an Eulerian frame of reference. Therefore, this approach is often referred to as Euler-Lagrange (EL) approach.[32] It has been first applied to gas-solid flows in the mid 90's.[33,34] For the EL approach direct numerical simulations of the continuous phase, i.e., a full resolution of all length scales (Nierhaus et al.[35]), as well as the filtered Navier-Stokes equations[36] have been reported. One of the first applications of the EL approach for bubbly flows was the work of Delnoij et al.[32] who solved the governing equations on a 2-D grid. In the same year Tomiyama et al.[37] reported a similar approach on a three-dimensional grid. The EL approach has been also extended to gassed stirred tanks. A recent example is the work of Arlov et al.[38] However, all of these studies are concerned with the multiphase flow only and do not focus on mixing or chemical reactions (see in the following) within the gas and/or liquid phase.

Since a full resolution of individual bubbles in a realistic system (there are approximately $1.5 \cdot 10^6$ bubbles/m^3 assuming a bubble diameter of 5 mm, and a gas holdup of 10%) is still computationally infeasible, the EL approach has significant potential of becoming the standard method for the detailed analysis of multiphase flow and mixing. This is because the modeling effort is lower compared the EE technique. For example, the change in bubble size due to coalescence and breakage of bubbles can be easily captured directly using the EL approach. In contrast, in the EE approach a separate PBE has to be solved for that purpose.

Nevertheless, several issues need to be addressed in the EL method, including (a) the development of more reliable schemes to map Lagrangian properties onto the Eulerian frame of reference and vice versa,[39] (b) a detailed treatment of bubble-wall and bubble-bubble collisions, (c) sophisticated modeling of the subgrid-scale velocity fluctuations,[40–42] as well as (d) the inclusion of coalescence phenomena.[27] In a recent example, Hu and Celik[39] published a LPT study for relatively large individual bubbles. For the backward coupling or Lagrange-to-Euler mapping (i.e., the forces exerted on the liquid phase by the bubbles), they used a novel approach called the "particle-source-in-ball" (PSI-ball) concept. Darmana[27] used a special approach in which it is possible for bubbles to become larger than individual cells of the Eulerian grid. He considered also the local liquid-phase volume fraction in the momentum equation, i.e., the replacement of the continuous

phase by dispersed bubbles. This more advanced treatment of the continuous phase dates back to the work of Delnoij et al.[32] When taking the continuous phase volume fraction into account, the EL approach can also be used to study dense bubble swarms, i.e., a high local gas holdup. To cope with the large number of bubbles in such cases, it is possible to track bubble clusters instead of individual bubbles.[17] Also, coalescence and breakage can be accounted for in the EL approach as discussed in this article.

In multiphase reactor, the understanding of the impact of the multiphase flow on the chemical reactions is another import aspect. As typically chemical reactions usually take place only in the liquid phase or on the surface of a solid catalyst, the correct prediction of mixing in the liquid phase is of great importance.[43] Hence, a quantification of micromixing (i.e., mixing on the smallest scales), mesomixing (i.e., mixing on intermediate scales) and macromixing (i.e., mixing on the reactor scale) is required to characterize and predict the performance of the reactor.

Over the past few years, several researchers have analyzed mixing and chemical reactions in multiphase systems. In the beginning, studies focused mostly on experimental techniques in single-phase systems, e.g., by the use of so-called Bourne reactions[44–47] or the reaction of iodine with tyrosine.[48] Frequently, competing reactions were used which yield different product distributions depending on the efficiency of micromixing.[49–51] Recent experimental methods in the field of multiphase mixing also include the tracking of radioactive particles.[52] Furthermore, conductance measurements in simple tracer experiments are still popular to study macromixing in bubble column reactors.[53–56] Other methods for the detection of tracers are summarized in the publication of Joshi.[57] However, these experiments provide only an integral picture of macromixing in these reactors. Micro- and mesomixing cannot be quantified.

In the area of micromixing in bubbly flows, the first computational studies on nondeformable 2-D bubbles were reported by Khinast[58] and later extended to fully deformable bubble swarms in complex fluids involving arbitrary chemical reactions.[24–26] Also, it became possible with the aid of massively parallelized computer software to study mass transfer around 3-D bubbles.[27] However, this work was limited to cases with unrealistically low Schmidt numbers ($Sc = 1$) in the continuous phase. In addition, it was shown that the results of these high-fidelity reactive micromixing simulations can be described to some extent by simplified models.[24] Also, recent studies of (micro-) mixing of a fluid with granular particles were reported,[59,60] encouraging future work in this area. However, a detailed analysis of mixing including mass transfer has not been reported,[59,60] and is also missing in most of the literature dealing with multiphase mixing.

Macromixing in bubble-column reactors was studied numerically by various researchers using virtual tracer experiments.[61,62] These simulations focus on the analysis of an inert tracer in the liquid phase, and, hence, are not involving the effects of mass transfer and reaction. Also, they are incapable — same as real tracer experiments — to quantify the local distribution of mixing, as well as the temporal fluctuation. Hence, a detailed multiscale quantification of the local distribution of mixing rates cannot be found in literature as of yet.

In summary, there has been significant progress in describing flow and mixing in multiphase systems at the micro- and macroscales. These studies focused mainly on an integral measure for mixing (e.g., an axial dispersion coefficient) or were concerned with microscale mixing. However, the quantification of mixing on the mesoscale, i.e., on the level of a bubble plume, has not been reported. Furthermore, nearly all of the experiments and simulations reported in literature were concerned with a tracer already dissolved in the liquid phase. Thus, conclusive results for the effect of mass transfer on the distribution of an inert scalar are scarce. An exception is the work of Darmana.[27] However, they did not investigate the effects of the process parameters on mixing and chemical reactions, nor did they model these effects. Consequently, the analysis of mixing involving mass transfer still requires a significant amount of research as systematic studies highlighting the interaction of mass transfer, mixing and chemical reactions in large bubble plumes are rare, especially for mesoscale effects. Even fundamental concepts describing these mesomixing effects and the interaction of mesomixing with the micro- and macroscales are still absent. Thus, it is the aim of this study is to provide the basis for such a concept.

Objectives

The objective of this article is to analyze in detail the flow, mixing and the chemical reactions in a bubbly flow, which are encountered in many industrial applications including bubble column reactors and bioreactors. Specifically, it is our goal to:

- perform validated, state-of-the-art simulations of large bubble swarms (up to 100,000 bubbles) including species transport and chemical reactions based on large eddy simulations (LES),
- study the numerical aspects of the simulation tool,
- apply our simulation code to highlight the relative importance of several parameters on inert and reactive mixing in large bubble swarms, and
- provide novel perspectives for a rigorous modeling of the mixing effects in bubble swarms.

For this purpose, we first present an advanced numerical method for analyzing in detail the multiphase flow and mixing in dilute bubble columns. Subsequently, we employ state-of-the-art tools for the analysis of mixing that we adopt from single-phase mixing studies. Thus, we can present for the first time a detailed picture of multiphase mixing in dilute bubble swarms by means of computer simulations. Also, we are the first that systematically analyze the effect of process parameters on inert and reactive mixing in large bubble swarms. Finally, we focused on the distribution of the scale of segregation in multiphase systems with and without mass transfer. This is a completely new aspect on how to analyze mixing in these complex systems.

Problem Formulation

Multiphase flow

In this work, we use an LES-based Euler-Lagrange method to study flow, mixing and reactions in an unstirred bubble columns. The momentum balance equations for

multiphase flow consist of the filtered incompressible Navier-Stokes equations for the liquid phase and Newton's equation of motion for the disperse phase. The boundary conditions for the filtered Navier-Stokes equations include the typical conditions for the liquid phase at the wall (no-slip, as well as closures for the subgrid-scale stress), as well as a perfect-slip condition at the top outlet of the bubble column (to mimic an inviscid gas-phase top layer). The interaction of the liquid phase with the disperse phase is incorporated via source terms in the momentum equation, i.e., we perform a full two-way coupling of the involved phases. The initial conditions for the disperse phase, i.e., Newton's equation of motion, consist of specified position and velocity at the inlet. At the boundaries we perform an inelastic bounce back of the disperse phase with a coefficient of restitution of 0.9.

Following Darmana[27] the filtered continuity and momentum balance equation for the continuous phase can be written as

$$\frac{\partial \varepsilon_{\mathrm{L}}}{\partial t} + \nabla \cdot (\varepsilon_{\mathrm{L}} \cdot \bar{\boldsymbol{u}}) = 0 \tag{1}$$

$$\frac{\partial \bar{\varphi}_{\mathrm{L}}}{\partial t} + \nabla \cdot (\bar{\varphi}_{\mathrm{L}} \bar{\boldsymbol{u}}) = -\varepsilon_{\mathrm{L}} \cdot \nabla \bar{p} - \nabla \cdot (\varepsilon_{\mathrm{L}} \cdot \bar{\tau}_{\mathrm{L}}) + \varepsilon_{\mathrm{L}} \cdot \rho_{\mathrm{L}} \cdot \boldsymbol{g} + \Phi \tag{2}$$

with

$$\bar{\varphi}_{\mathrm{L}} = \varepsilon_{\mathrm{L}} \cdot \rho_{\mathrm{L}} \cdot \bar{\boldsymbol{u}} \tag{3}$$

Here ρ_{L} is the (constant) liquid density, ε_{L} is the liquid-phase volume fraction, and $\bar{u}$ is the filtered velocity vector of the liquid phase. Note, that we have neglected the mass transfer between the two phases in the continuity equation (Eq. 1) since its contribution is very small. This is due to the fact that we concentrate on dilute bubble swarms, and, hence, mass-transfer rates for reactive, as well as nonreactive systems are typically negligible compared to the total liquid mass in these systems. In the momentum equation Eq. 2, $\bar{\varphi}_{\boldsymbol{L}}$ is the filtered liquid-phase mass flux, $\bar{p}$ is the resolved pressure, $\bar{\tau}_{\mathrm{L}}$ is the liquid-phase stress tensor, $\boldsymbol{g}$ is the gravitational acceleration vector, and Φ is the volume-specific coupling force exerted by the dispersed phase (see the Numerics section of this article).

The liquid-stress tensor needs additional modeling. Here, we use the eddy viscosity concept and calculate the total stress from an effective viscosity

$$\bar{\tau}_{\mathrm{L}} = -\mu_{\mathit{eff},L} \cdot \left[(\nabla \bar{\boldsymbol{u}} + \nabla \bar{\boldsymbol{u}}^T) - \frac{2}{3} \cdot \boldsymbol{I} \cdot (\nabla \cdot \bar{\boldsymbol{u}}) \right] \tag{4}$$

The effective viscosity is the sum of the molecular and subgrid-scale viscosity in the liquid phase $\mu_{\mathrm{SGS,L}}$

$$\mu_{\mathrm{eff,L}} = \mu_{\mathrm{L}} + \mu_{\mathrm{SGS,L}}. \tag{5}$$

In most of our simulations the turbulent viscosity is calculated from a simple algebraic model, i.e., the standard Smagorinsky model

$$\mu_{\mathrm{SGS,L}} = \rho_{\mathrm{L}} \cdot (C_s \cdot \Delta)^2 \cdot |\bar{\boldsymbol{S}}|. \tag{6}$$

Here, C_s is the Smagorinsky constant with a typical value of 0.1,[27] Δ is the filter length, and $|\bar{\boldsymbol{S}}|$ is the magnitude of the filtered strain rate tensor. The filtered strain rate tensor is defined as

$$\bar{\boldsymbol{S}} = \frac{1}{2} \cdot (\nabla \bar{\boldsymbol{u}} + \nabla \bar{\boldsymbol{u}}^T). \tag{7}$$

The implementation in our code for the calculation of $\mu_{SGS,L}$ is slightly different from Eq. 6 as we first calculate the subgrid-scale kinetic energy k from Eq. 8. This implementation enables a separate calculation of k and $\mu_{\mathrm{SGS,L}}$, which can be useful for comparison purposes

$$k = \frac{2 \cdot C_k}{C_e} \cdot \Delta^2 \cdot |\bar{\boldsymbol{S}}|^2 \tag{8}$$

In Eq. 8, C_k and C_e are model constants.

Having calculated k, the subgrid-scale viscosity is calculated from

$$\mu_{\mathrm{SGS,L}} = \rho_{\mathrm{L}} \cdot C_k \cdot \sqrt{k} \cdot \Delta \tag{9}$$

After substituting Eq. 8 in Eq. 9, we recover Eq. 6 with the relation

$$C_s = \left(\frac{2 \cdot C_k^3}{C_e} \right)^{1/4} \tag{10}$$

In addition to the algebraic model, we have used a more advanced differential subgrid-scale model to account for nonresolved turbulent fluctuations. The one-equation model used in this work solves the following differential equation for the subgrid-scale kinetic energy k[63]

$$\frac{\partial k}{\partial t} + \nabla \cdot (k \bar{\boldsymbol{u}}) = \nabla \cdot \left(\frac{\mu_{\mathit{eff},L}}{\rho_{\mathrm{L}}} \cdot \nabla k \right) - \varepsilon - \bar{\tau}_{\mathrm{L}} : \bar{\boldsymbol{S}} \tag{11}$$

Here ε is the subgrid-scale energy dissipation given by

$$\varepsilon = \frac{C_\varepsilon \cdot k^{3/2}}{\Delta} \tag{12}$$

The subgrid-scale viscosity is then calculated according to Eq. 9. When using these algebraic and differential subgrid-scale models, we exclude the effect of bubble motion on the generation of the subgrid-scale fluctuations, i.e., so-called bubble induced turbulence (BIT). The influence of BIT on the subgrid-scale viscosity could be modeled by using (for example) the model of Sato and Sekoguchi.[64] However, the studies of Deen et al.,[36] as well as of Niceno et al.[65] indicate only marginal effects of BIT on the mean and fluctuating flow field in dilute bubble swarms. Hence, the exclusion of BIT from our simulations is justified and in line with previous work published in that field.[27,39] In our work, we use wall functions for the computation of the subgrid-scale viscosity near the no-slip boundaries. This treatment of the walls can be used for a wide range of dimensionless wall

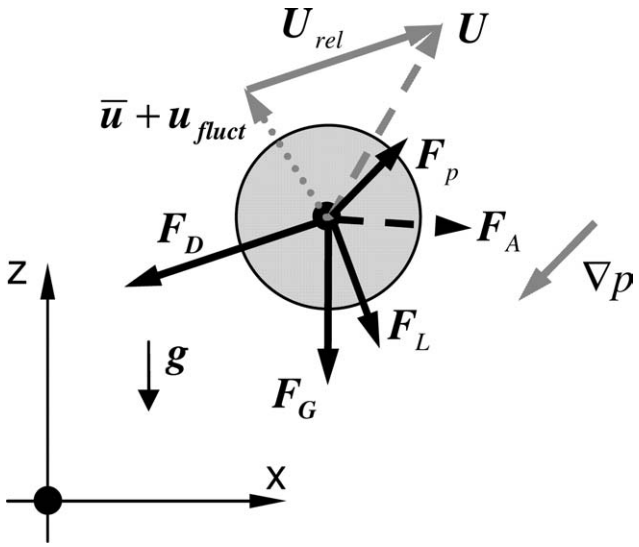

Figure 1. Forces acting on a particle.

distances, as it incorporates the velocity profile from the laminar, to the buffer and the fully turbulent region.[63] We specifically use the following (implicitly-defined) dimensionless velocity profile near the wall, which was initially introduced by Spalding[66]

$$y^+ = u^+ + \frac{1}{E}\cdot\left[\exp[\kappa\cdot u^+] - 1 - \kappa\cdot u^+ - \frac{1}{2}\cdot(\kappa\cdot u^+)^2 - \frac{1}{6}\cdot(\kappa\cdot u^+)^3\right] \tag{13}$$

Here, $y^+ = y_0 \cdot u_\tau/\nu$ and $u^+ = \bar{u}_0/u_\tau$ denote the dimensionless wall distance and the dimensionless velocity profile, respectively. y_0, u_τ, $\bar{u}_0$ and ν are the wall normal distance of the first computational cell near the wall, the friction velocity, the filtered wall parallel velocity in the first computational cell near the wall, and the kinematic velocity of the liquid phase, respectively. In our code we directly insert the definition of the nondimensional variables y^+ and u^+ in Eq. 13 to obtain a nonlinear equation for u_τ. Using an initial guess for u_τ, we then solve iteratively for the friction velocity using a Newton algorithm. The wall-shear stress can then be calculated directly out of u_τ. Details of this procedure can be found in deVilliers.[63]

Newton's equation of motion for each individual bubble is (see Figure 1)

$$m_p \cdot \frac{d\mathbf{U}}{dt} = \mathbf{F_G} + \mathbf{F_p} + \mathbf{F_D} + \mathbf{F_L} + \mathbf{F_A} \tag{14}$$

Here m_p is the mass of the particle, i.e., the bubble, $\mathbf{U}$ is the velocity vector of the bubble, $\mathbf{F_G}$ is the gravity force, $\mathbf{F_p}$ is the force due to a pressure gradient, $\mathbf{F_D}$ is the drag force, $\mathbf{F_L}$ is the lift, and $\mathbf{F_A}$ is the added-mass force. The models for each of these forces are summarized in Table 1. Throughout our work, we assume that the spin of the bubble is equal to the fluid spin surrounding the bubble. This is justified by the very low density of the gas inside the bubble, resulting in a negligibly small moment of inertia of the bubble. Thus, we do not need to solve the conservation equation for rotational momentum, hence, saving computation time and memory. In our work, we use the standard drag curve[67] for a rigid sphere to account for the drag forces the bubble experiences. This is thought to represent the conditions in experimental systems (e.g., that of Becker[68]) reported in literature best, since already small amounts of contaminations in the liquid phase cause bubbles to behave like rigid spheres. The model used for the lift force dates back to the PhD thesis of Auton[69] and takes into account forces due to velocity gradients, i.e., vorticity, in the liquid phase. This model is valid for homogeneous bubble flows, i.e., for cases where both bubble radius and liquid-phase vorticity are small.[32,70] It is well established for Euler-Lagrange modeling of gas-liquid flows (see for example Darmana[27]). Note that we neglect Magnus lift forces as we already assumed identical rotation rates of the bubbles and the surrounding liquid. The model for the added mass force was adapted from Hu and Celik,[39] and is suitable for describing this type of forces in dilute bubble swarms. The lift and added mass coefficient were chosen as $C_L = 0.53$ (based on Auton[69]), and $C_A = 0.5$ (based on Hu and Celik[39]), respectively. In our work, we have neglected the Basset history forces, since it has been shown by both simulations,[71] as well as experiments[72] that it is negligibly small in the flow of small bubbles around 1 mm. In Eq. 14 d/dt refers to the substantial derivative along the particle trajectory. More details on the procedures of how to obtain the values of relevant variables at the bubble position are detailed in the Numeric's section.

Species transport

The species conservation equation for species i in the liquid phase is

$$\frac{\partial(\varepsilon_L\cdot\bar{Y}_i)}{\partial t} + \nabla\cdot(\varepsilon_L\cdot\bar{\boldsymbol{u}}\bar{Y}_i) = \nabla\cdot(\varepsilon_L\cdot D_{eff,i}\cdot\nabla\bar{Y}_i) + \Phi_{\dot{N}_i} + \varepsilon_L\cdot\sum_j \nu_{i,j}\cdot r_j + \bar{Y}_i\cdot\frac{\partial(\varepsilon_{L,mean})}{\partial t} \tag{15}$$

$$D_{eff,i} = D_i + \frac{\mu_{eff,L}}{\rho_L\cdot Sc_{SGS}} \tag{16}$$

Here $\bar{Y}_i$ is the filtered concentration of species i in the liquid phase, D_i is the molecular diffusion coefficient, and

Table 1. Force Models used for the Lagrangian Particle Tracking

Force	Model Equation
$\mathbf{F_G}$	$m_p\cdot\boldsymbol{g}$
$\mathbf{F_p}$	$-V_p\cdot\nabla\bar{p}$
$\mathbf{F_D}$	$-C_D\cdot\frac{1}{2}\rho_L\cdot\lvert\mathbf{U_{rel}}\rvert\cdot\mathbf{U_{rel}}\cdot A_{cross}$,
	$\mathbf{U_{rel}} = \boldsymbol{U} - (\bar{\boldsymbol{u}} + \boldsymbol{u}_{\mathbf{fluct}})$,
	$C_D = \begin{cases} 24/Re_p\cdot\left(1 + 0.15\cdot Re_p^{0.687}\right), & Re_p \le 800 \\ 0.44, & Re_p > 800 \end{cases}$
	$Re_p = \frac{\lvert U_{rel}\rvert\cdot d_p\cdot\rho_L}{\mu_L}$
$\mathbf{F_L}$	$-C_L\cdot\rho_L\cdot V_p\cdot\mathbf{U_{rel}}\times\omega, \omega = \nabla\times\bar{\boldsymbol{u}}$
$\mathbf{F_A}$	$-C_A\cdot\rho_L\cdot V_p\cdot\frac{d}{dt}\mathbf{U_{rel}}$

Sc_{SGS} is the subgrid-scale Schmidt number. The last term in Eq. 15 accounts for the artificial addition/removal of the liquid phase to ensure the overall conservation of the two-phase mixture in the computational domain (refer to the Numeric's section for more details). Furthermore, $\nu_{i,j}$ is the stoichiometric coefficient of reactant i in the homogeneous liquid-phase reaction j, and r_j is the reaction rate of reaction j. A value of $Sc_{SGS} = 0.7$ is used in most of the simulations performed in this work, as this value is frequently reported in numerous computational studies on scalar mixing. However, there is significant discussion regarding the value of the subgrid-scale Schmidt number for LES depending on the flow situation. Unfortunately, LES studies investigating this parameter are scarce. For example, a value of $Sc_{SGS} = 0.5$ has been suggested by Tominaga and Stathopoulos.[73] Others used the molecular Schmidt number (Darmana[27] as well as Feng et al[74]) or suggested $Sc_{SGS} = 0.4$ (Fox[75]). Consequently, we have investigated the impact of Sc_{SGS} on our calculations for mixing (see the Results section).

The volumetric source term $\Phi_{\dot{N}_i}$ is related to the mass-transfer rate from the bubble swarm according to

$$\Phi_{\dot{N}_i} = \frac{\partial \dot{N}_i}{\partial V} \tag{17}$$

Here ∂V is the differential volume on the Eulerian grid, and $\partial \dot{N}_i$ is the differential mass transfer from the disperse phase to this differential volume. The differential mass transfer $\partial \dot{N}_i$ depends on the local properties of the surrounding liquid. It can be calculated by the sum over all particles in the differential volume ∂V

$$\partial \dot{N}_i = \sum_z \partial A_{p,z} \cdot \beta_z(Re_{p,z}, Sc_i) \cdot (Y_{eq,i} - \bar{Y}_{\mathrm{amb},i,z}) \tag{18}$$

Here z is the particle index of all particles in the volume, is the interfacial area of particle z in the volume ∂V, β_z is the mass-transfer coefficient of particle z, $Re_{p,z}$ is the particle Reynolds number of particle z, $Y_{\mathrm{eq},i}$, is the equilibrium concentration of species i at the gas-liquid interface, and $\bar{Y}_{\mathrm{amb},i,z}$ is the ambient concentration of species i near particle z in the liquid phase.

For spherical particles (i.e., the assumption in our work), the mass-transfer term simplifies to

$$\begin{aligned}\partial A_{p,z} \cdot \beta_z(Re_{p,z}, Sc_i) \cdot (Y_{\mathrm{eq},i} - \bar{Y}_{\mathrm{amb},i,z}) \\ = d_{p,z} \cdot \pi \cdot D_i \cdot Sh_{i,z}(Re_{p,z}, Sc_i) \cdot (Y_{\mathrm{eq},i} - \bar{Y}_{\mathrm{amb},i,z})\end{aligned} \tag{19}$$

when assuming that the total interfacial area of particle z is in the volume ∂V, i.e., $\partial A_{p,z} = A_{p,z}$. The standard definition[76] of the Sherwood number $Sh_{i,z}$ has been used in this work.

Reaction model

We have implemented a reaction model involving j independent reactions. The reaction kinetics of each of these reactions are modeled as Michaelis-Menten kinetics, i.e.

$$r_j = k_j \cdot \prod_k \frac{\bar{Y}_k^{e_{kj}}}{K_{kj} + \bar{Y}_k^{E_{kj}}} \tag{20}$$

Here k_j is the rate constant of reaction j, k is the running index for all species, e_{kj} and E_{kj} are the reaction exponents of species k in reaction j, and K_{kj} is a reaction constant for species k in reaction j. With this reaction model we are able to study complex reaction networks with arbitrary order of reaction, which are typical for biochemical reactions. As we use only filtered concentrations without a closure for small-scale mixing, we do not take micromixing effects stemming from the nonlinearity of the reactions into account.[77,78] This assumption is justified, as long as the characteristic reaction time is larger than the micromixing time, i.e., the time it takes for concentration variances on the subgrid scale to vanish. For the relatively slow reactions studied in this work, this is assumption is valid.

Numerics

We use the open-source CFD package "OpenFOAM"[79] which is designed for parallel computing, and, hence, is a good basis for future extension to very large systems containing significantly more individual bubbles. OpenFOAM uses a finite volume discretization, and offers a large number of numerical schemes for discretizing partial differential equations.[80] In the next few paragraphs we discuss our advanced mapping procedures and our new strategy to solve the multiphase flow equations. Also, we shortly comment on some details of the species transport and the bubble tracking algorithm.

Mapping procedures

Lagrangian-to-Euler Mapping. To recover the liquid-phase fraction ε_L in each computational cell, the volume fraction of each individual bubble in this cell has to be known. For arbitrary shapes of the bubble and the cell this is computationally very expensive. Hence, an idealized shape of the bubble has to be assumed. For example, Darmana[27] used a cubic approximation of each bubble, as this shape allows a computationally efficient calculation and seems to represent the bubble shape reasonably well. However, it is difficult to account for noncubic cells of an arbitrary grid, restricting the method to simple rectangular Cartesian grids.

Another approach has been reported by Hu and Celik[39] for the mapping of Lagrangian sources terms onto an Eulerian grid. In their particle-in-cell-ball (PSI-ball) method they use the distances between the centers of surrounding cells within a defined influence radius, and the particle center as a basis for their distribution. In this method the inverse of these distances corresponds to the weight of the Lagrangian source terms in each individual cell.

In our work, we use a more sophisticated approach to recover the Lagrangian properties, i.e., the local liquid-phase volume fraction, the momentum source term, as well as the species source term on the Eulerian grid. While parts of our method have been in use for some years, our numerical implementation results in a better accuracy and reduced computational time. Our approach consists of three steps, i.e., (a) the determination of the cells that are in the range of the bubble, (b) the calculation of a virtual overlapping volume of the bubble with each individual surrounding cell, and (c) the distribution of the Lagrangian properties among the

surrounding cells. For the first step we scan all surrounding cells and check if the distance x_{dist} between the cell center and the particle center is smaller than

$$x_{\text{dist}} < \frac{d_p}{2} + x_{\text{cell,max}}. \tag{21}$$

This is essential to save computational time as the calculation of the virtual overlapping volume (see later) is time-consuming. An additional feature of our implementation is that the surrounding cells are determined before the calculation starts. This information is then saved and loaded at each time step. Hence, we avoid searching for all surrounding cells, which may become limiting for large arbitrary grids. In Eq. 21, the variable $x_{\text{cell,max}}$ is the maximum distance from the cell center to a cell's boundary point. It has to be calculated and saved for each individual cell. As we have used uniform rectangular grids in our work, $x_{\text{cell,max}}$ corresponds to $\sqrt{3/4}$ of the cell length. For step (b), i.e., the overlap calculation, we use a fourth-order template function similar to Deen et al.[81] The half length for this calculation was set to 1.5 bubble diameters. Hence, the computed overlap is not a physically correct overlap of the bubble with the surrounding cell, but a virtual overlap that characterizes the influence of the bubble on this cell. Finally, we distribute the Lagrangian properties among the surrounding cells according to their relative virtual overlapping volumes with the particle. This guarantees that Lagrangian properties are conserved during the mapping. Also, our methodology yields a sufficiently smooth distribution of the Lagrangian properties on the Eulerian grid. However, care must be taken during the distribution of the particle volume. We had to impose a lower bound on the liquid-phase void fraction ε_L, as otherwise the filtered Navier-Stokes equation cannot be solved efficiently. We set the lower bound of ε_{L} equal to 0.05 as proposed by Darmana.[27]

Euler-to-Lagrangian Mapping

The Euler-to-Lagrangian mapping is the interpolation of the solution on the Eulerian grid at discrete particle locations. Previous studies[27,32,37] frequently employed a simple linear interpolation at the center position of the particle. This is problematic to some extent, as the particles have a physical size, and, therefore, the value at the particle center may not appropriately represent their environment. Furthermore, problems with this approach have been shown by Darmana[27] in the form of spurious oscillations in the rise velocity of a single bubble. Our analysis shows that these oscillations originate from the fact that a relatively coarse Eulerian mesh is used in EL simulations onto which the interface terms are imposed. This results in a poor resolution of the effect of these forces on the Eulerian grid. For example, it has significant impact on the velocity field whether the particle is completely in one cell or it is crossing a cell boundary. In the latter case the force is distributed among two or more cells. Thus, the peak velocity is significantly smaller than in the former case, and a slightly oscillating velocity field is obtained. Consequently, even the best interpolation algorithm leads to oscillations of the bubble's rise velocity. Although this effect can be somewhat alleviated by the Lagrangian-to-Euler mapping, these oscillations are directly transferred during the mapping procedure using conventional linear interpolation at the particle center position. In this work, we again use the virtual overlapping volumes from the Lagrangian-to-Euler mapping procedure to map Eulerian quantities at the particle position. The value at the particle position was obtained by summation of the product of the relative overlapping volume and the cell center value over all surrounding cells. This strategy turned out to give only insignificant bubble-rise velocity oscillations and was computationally efficient, as the relative overlapping volumes were already computed during the Lagrangian-to-Euler mapping.

Multiphase flow solver

The numerical solution procedures for solving the multiphase flow equations have been adopted from existing literature on the EE[82] and the EL approach.

In the EE approach usually the pressure-implicit-split-operator (PISO) algorithm[83] is adopted to solve for the pressure-velocity coupling. Also, the momentum equation is frequently divided by the phase fraction to obtain a "phase-intensive" momentum equation.[82] This is beneficial for the numerical solution procedure, as numerical noise is suppressed at low-phase fractions. Thus, the momentum equation can be transformed into (refer to Crowe et al.[33])

$$\begin{aligned}\varepsilon_{\text{L}} \cdot \rho_{\text{L}} \cdot \frac{\partial(\bar{\boldsymbol{u}})}{\partial t} + \varepsilon_{\text{L}} \cdot \rho_{\text{L}} \cdot \nabla \cdot (\bar{\boldsymbol{u}}\bar{\boldsymbol{u}}) + \rho_{\text{L}} \cdot \bar{\boldsymbol{u}} \frac{\partial(\varepsilon_{\text{L}})}{\partial t} \\ + \rho_{\text{L}} \cdot \bar{\boldsymbol{u}} \cdot \nabla \cdot (\varepsilon_{\text{L}} \bar{\boldsymbol{u}}) = -\varepsilon_{\text{L}} \cdot \nabla \bar{p} - \nabla \cdot (\varepsilon_{\text{L}} \cdot \bar{\tau}_{\text{L}}) \\ + \varepsilon_{\text{L}} \cdot \rho_{\text{L}} \cdot \boldsymbol{g} + \Phi\end{aligned} \tag{22}$$

Taking into account the continuity equation, the third and fourth term on the lefthand side vanish. After division by ε_{L} and ρ_{L}, we obtain the phase-intensive momentum equation for the liquid phase

$$\begin{aligned}\frac{\partial \boldsymbol{u}}{\partial t} + \nabla \cdot (\bar{\boldsymbol{u}}\bar{\boldsymbol{u}}) = -\nabla \frac{\bar{p}}{\rho_{\text{L}}} + \frac{1}{\varepsilon_{\text{L}}} \cdot \nabla \\ \times \left[\varepsilon_{\text{L}} \cdot \nu_{\text{eff,L}} \cdot \left(\nabla \bar{\boldsymbol{u}} + \nabla \bar{\boldsymbol{u}}^T - \frac{2}{3} \cdot \boldsymbol{I} \cdot (\nabla \cdot \bar{\boldsymbol{u}}) \right) \right] \\ + \boldsymbol{g} + \frac{\Phi}{\varepsilon_{\text{L}} \cdot \rho_{\text{L}}}\end{aligned} \tag{23}$$

Note that $\bigtriangledown \cdot \bar{\boldsymbol{u}}$ is not equal to zero in our case, and that $\boldsymbol{I}$ represents the identity matrix. This equation can be solved directly imposing appropriate boundary conditions. Since the hydrostatic pressure gradient may be significant, we exclude this contribution from the momentum equation by defining a modified pressure gradient according to

$$\nabla \bar{p}* = \nabla \bar{p} - \rho_{\text{L}} \cdot \boldsymbol{g} \tag{24}$$

The boundary condition for $\bar{p}$* can then be approximated by a zero gradient for static, impermeable walls. In our work, the final momentum equation for the liquid phase that is solved together with the continuity equation (Eq. 1) is

$$\frac{\partial \bar{\boldsymbol{u}}}{\partial t} + \nabla \cdot (\bar{\boldsymbol{u}}\bar{\boldsymbol{u}}) = -\nabla \bar{p}' + \frac{1}{\varepsilon_L} \cdot \nabla \cdot \left[\varepsilon_L \cdot \nu_{\text{eff,L}} \cdot \left(\nabla \bar{\boldsymbol{u}} + \nabla \bar{\boldsymbol{u}}^T - \frac{2}{3} \cdot \boldsymbol{I} \cdot (\nabla \cdot \bar{\boldsymbol{u}}) \right) \right] + \frac{\Phi}{\varepsilon_L \cdot \rho_L} \quad (25)$$

Here we have abbreviated the pressure gradient term by the definition

$$\nabla \frac{\bar{p}^*}{\rho_L} = \nabla \bar{p}' \quad (26)$$

During the simultaneous solution of Eqs. 1 and 25, the liquid-phase volume fraction on the Eulerian grid is known as this information is obtained after the Lagrangian-to-Euler mapping. Thus, the first term on the lefthand side of Eq. 1, i.e., the time derivative of the liquid-phase volume fraction is known explicitly. Hence, most of the numerical algorithm that is used for incompressible flow may be used. In this work the PISO algorithm is adopted. Details of this algorithm for single-phase flows can be found in the original work of Issa,[83] as well in the publications of Nilsson[84] and Kaerrholm.[85] Here we focus on the handling of the velocity-pressure coupling only, i.e., the heart of the solution algorithm. The discretized momentum equation (Eq. 25) has the general shape

$$a_P^u \cdot \bar{\boldsymbol{u}}^P + \sum_N a_N^u \cdot \bar{\boldsymbol{u}}^N = \boldsymbol{r} - \nabla \bar{p}' \quad (27)$$

Here a_P^u and a_N^u are the diagonal and off-diagonal coefficients in the system of algebraic equations, respectively. These vectors are obtained during the discretization of the momentum equation. The vectors $\bar{\boldsymbol{u}}^P$ and $\bar{\boldsymbol{u}}^N$ are the velocity vectors at the cell center P and at the neighboring cells, respectively. The vector $\boldsymbol{r}$ incorporates the known part of the system, i.e., the force from the dispersed phase Φ, as well as the viscous part (second term on the righthand side of Eq. 25). Next, we define an operator $\boldsymbol{H}(\bar{\boldsymbol{u}})$ as follows

$$\boldsymbol{H}(\bar{\boldsymbol{u}}) = \boldsymbol{r} - \sum_N a_N^u \cdot \bar{\boldsymbol{u}}^N \quad (28)$$

Hence, the velocity at the cell center point P can be calculated from

$$\bar{\boldsymbol{u}}^P = (a_P^u)^{-1} [\boldsymbol{H}(\bar{\boldsymbol{u}}) - \nabla \bar{p}'] \quad (29)$$

By multiplication with ε_L, and applying the continuity equation (Eq. 1), we obtain the following expression for the pressure

$$\nabla \cdot [\varepsilon_L \cdot (a_P^u)^{-1} \nabla \bar{p}'] = \nabla \cdot [\varepsilon_L \cdot (a_P^u)^{-1} \boldsymbol{H}(\bar{\boldsymbol{u}}_L)] + \frac{\partial \varepsilon_L}{\partial t} \quad (30)$$

In this equation the righthand side is known from the previous calculation steps of the PISO algorithm, and the resulting equation can be solved for the unknown pressure $\bar{p}'$. For this purpose we use fast geometric-algebraic multi-grid (GAMG) solvers with preconditioning.[79] Finally, the velocity $\bar{\boldsymbol{u}}^P$ at each point P can be calculated using Eq. 29.

The aforementioned algorithm together with no-slip and perfect-slip boundary conditions works for the special case where the mean liquid-phase void fraction is constant over time, i.e., the amount of liquid phase in the computational domain does not change. However, in this work bubbles are continuously entering and leaving the bubble column, and, consequently, the total gas-phase volume and the mean liquid-phase void fraction fluctuate over time, leading to a variable fill level of the two-phase mixture in the bubble column. Therefore, in conventional Euler-Euler simulations a top layer of the disperse phase, e.g., the gas phase, together with appropriate boundary conditions is used to capture the fluctuations of the fill level. However, in this work we do not use a top layer of the gas phase as we reconstruct the distribution of ε_L directly from the particle (bubble) positions. As we use a fixed grid, we solve all equations for a fixed amount of the two-phase mixture. Hence, we have to account for in- and outflow of the liquid phase as a consequence of net out- and inflow of the gas phase. In the previous work of Darmana,[27] for example, this problem was solved by using "pressure cell slits" on top of the computational domain. Due to these prescribed pressure cells, hydrodynamic instabilities at the surface have been reported. These instabilities were suppressed using a certain geometrical configuration of the pressure cell slits.[27] In this work, we follow a more advanced approach, in which we subtract the net change of the void fraction in the column from the continuity equation of the liquid phase. To the best of our knowledge, this approach is new and has not been documented in literature before. Thus, we subtract or add liquid volume uniformly over the whole computational domain whether the mean liquid-phase void fraction decreases or increases, respectively. By doing so, we fully preserve the local effects of the changing void fraction on the one hand and deal in an elegant way with the displacement of liquid-phase volume on the other hand. The reformulated continuity equation is

$$\frac{\partial \varepsilon_L}{\partial t} + \nabla \cdot (\varepsilon_L \cdot \bar{\boldsymbol{u}}) = \frac{\partial \varepsilon_{L,\text{Mean}}}{\partial t} \quad (31)$$

Hence, the pressure equation that we solve for is

$$\nabla \cdot [\varepsilon_L \cdot (a_P^u)^{-1} \nabla \bar{p}'] = \nabla \cdot [\varepsilon_L \cdot (a_P^u)^{-1} \boldsymbol{H}(\bar{\boldsymbol{u}}_L)] + \frac{\partial \varepsilon_L}{\partial t} - \frac{\partial \varepsilon_{L,\text{Mean}}}{\partial t} \quad (32)$$

The term $\partial \varepsilon_{L,\text{Mean}}/\partial t$ can be evaluated explicitly from the known local distribution of ε_L by volume averaging. This method has the advantage that we avoid discrete locations where liquid flows out of the domain. Consequently, we do not observe any instability. However, this artificial addition and removal of the liquid phase has to be taken into account when solving the species transport equation.

The schemes for discretizing the convection terms were second-order accurate. We have used the implicit Euler time integration scheme with a time step giving a maximum Courant number of approximately 0.3.

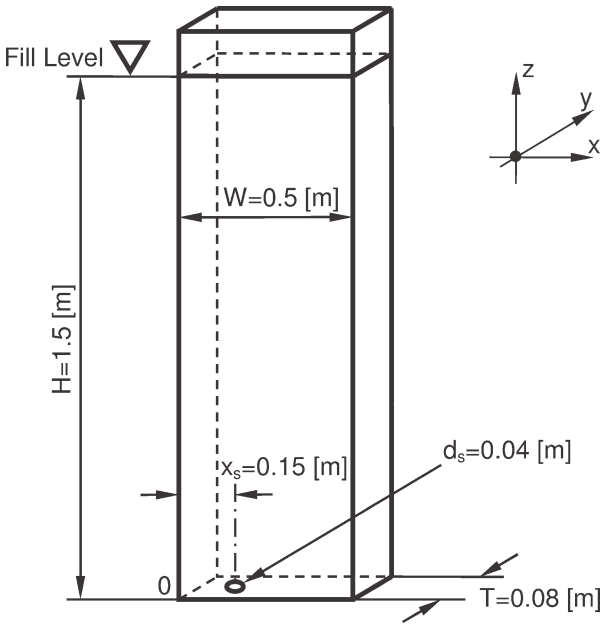

Figure 2. Geometrical setup of the "Becker" case.

Species transport

The volumetric source terms $\Phi_{\dot{N}_i}$, as well as the chemical source term in the species transport equation Eq. 15 were treated explicitly. All other terms were discretized implicitly. For the convective term a second-order accurate scheme was used. The boundary conditions were set to zero gradient for all walls and the top surface.

Bubble tracking

Newton's equation of motion was solved after manipulation and introducing the density ratio $\gamma_\rho = \rho_p/\rho_L$ in the following form

$$\frac{d\boldsymbol{U}}{dt} = \frac{\gamma_\rho}{\gamma_\rho + C_A}\cdot\boldsymbol{g} - \frac{1}{\gamma_\rho + C_A}\cdot\frac{\nabla\bar{p}}{\rho_L} - \frac{3}{4}\frac{C_D}{d_p}\cdot\frac{1}{\gamma_\rho + C_A}\cdot|\boldsymbol{U}_{\mathbf{rel}}| \times \boldsymbol{U}_{\mathbf{rel}} - C_L\cdot\frac{1}{\gamma_\rho + C_A}\boldsymbol{U}_{\mathbf{rel}}\times\omega + C_A\cdot\frac{1}{\gamma_\rho + C_A}\cdot\frac{d}{dt}(\bar{\boldsymbol{u}} + \boldsymbol{u}_{\mathbf{fluct}}) \tag{33}$$

The subgrid-scale fluctuating velocities $\boldsymbol{u}_{\mathrm{flcut}}$ were set to zero, as it can assumed (based on previous work[39,81]) that this will not have a substantial effect on the solution.

The details of the particle tracking routine are described in the PhD thesis of Kaerrholm.[85] In this face-to-face technique each individual bubble "knows" when it is crossing a cell face, and, hence, the source terms for each computational cell can be treated accurately. Using this approach, the particle cannot cross a cell boundary without exchanging momentum and mass with it. A more detailed description of the numerical details can be found in MacPherson et al.[86]

The following discretization of Eq. 33 was used:

- $\frac{d\boldsymbol{U}}{dt} \approx \frac{\boldsymbol{U}^{n+1}-\boldsymbol{U}^n}{\Delta t}$ (i.e., explicit Euler integration);
- $\nabla\bar{p}$ is calculated using a selectable gradient scheme;
- ω is calculated using a selectable gradient scheme.

The time step for the bubble tracking routine is user-selectable and was chosen as $1/10^{\mathrm{th}}$ of the time step used for integrating the filtered Navier-Stokes equations.

The total force acting from the bubble on the surrounding liquid is the opposite from the sum of the drag, lift, and added mass force that is exerted onto the bubble. Hence, the volumetric source term Φ is the sum over all particles i in the pertaining cell j

$$\Phi_j = \frac{\sum_i -(\boldsymbol{F}_{D,i} + \boldsymbol{F}_{L,i} + \boldsymbol{F}_{A,i})}{\Delta V_{\mathrm{cell,j}}} \tag{34}$$

Table 2. Process Parameters for the EL Simulations (Base Case)

Parameter	Abbreviation	Value
Particle size	d_p	1.6 [mm]
Gas feed rate	V_G	1.6 [L/min]
Liquid-phase viscosity	ν_L	$1\cdot10^{-6}$ [m^2/s]
Diffusion coefficient	D_i	$2\cdot10^{-9}$ [m^2/s]

Results

Multiphase flow

Setup. In this study, we have selected the "Becker" case[39] as a reference for our computations. The setup consists of a quasi-2-D unstirred bubble column, where gas enters a water-filled rectangular box through an excentric sparger (sparger dia. d_s = 0.04 m, distance from the left wall x_s = 0.15 m). The geometrical setup is illustrated in Figure 2, and the system parameters are listed in Table 2. It has to be noted here, that in the article of Becker[68] a bubble-size distribution has not been documented. Furthermore,

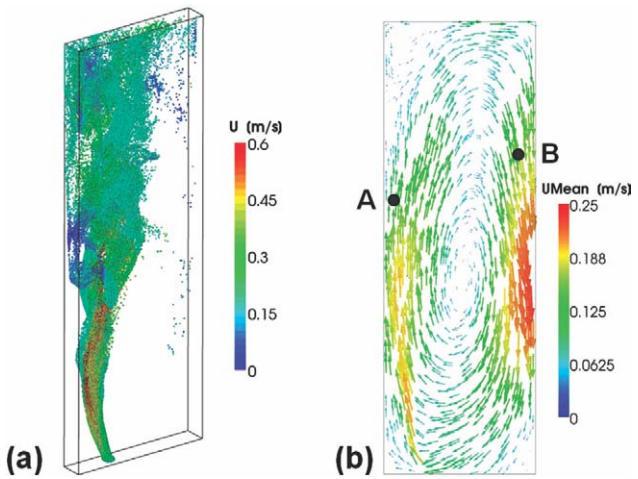

Figure 3. Principal flow fields in the bubble column: (a) snapshot of the instantaneous bubble distribution (bubbles are colored according to their velocity), and (b) time-averaged liquid-phase velocity distribution in the bubble column (points A and B indicate the probing locations for Figure 4).

[Color figure can be viewed in the online issue, which is available at wileyonlinelibrary.com.]

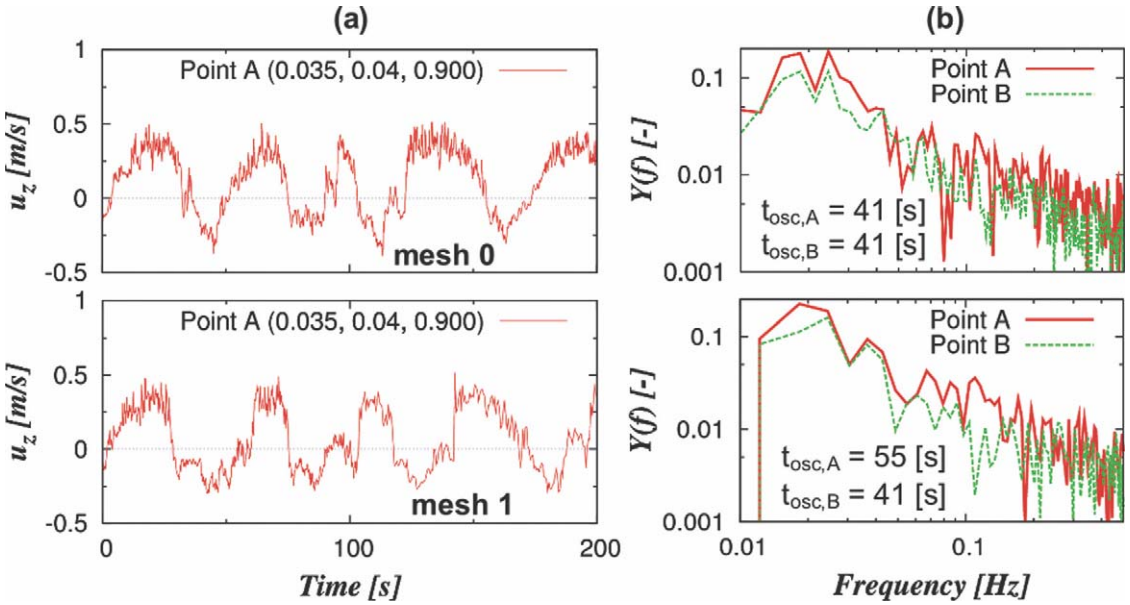

Figure 4. Time profiles at probing location A (a), and power spectrum of the time profile at probing location A and B (b) (Probing locations according to Figure 3; top: LES with coarse mesh "mesh 0", bottom: LES with fine mesh "mesh 1").

[Color figure can be viewed in the online issue, which is available at wileyonlinelibrary.com.]

in the Euler-Euler simulations of Sokolichin and Eigenberger[87] only a constant slip velocity (assumed to be 0.2 m/s) has been used to model bubbles with a mean diameter between 1 and 10 mm. Hence, a mean bubble diameter had to be selected in our work, due to the lack of further information. Our choice of monodisperse bubbles with a size of 1.6 mm is in accordance with the work of Hu and Celik,[39] which yields a terminal rise velocity of 0.172 m/s, and is the range specified by Sokolichin and Eigenberger.[87] Also, it has been shown by Diaz et al.[88] that for low-superficial gas velocities (ca. below 1 cm/s) the use of monodisperse bubbles is sufficient to reproduce experimental results for gas holdup and the plume oscillation period. The selection of the gas-feed rate, as well as of viscosity and diffusion coefficient, in accordance with previous experimental[68] and theoretical[87] work in this field. The box has a width of W = 0.5 m, a depth of 0.08 m, and is filled with liquid phase (water) up to a level of 1.5 m. Due to the excentric sparger, a nonhomogeneous distribution of the gas bubbles is observed and an unsteady circulation loop develops in the bubble column. The time-averaged liquid-phase flow field obtained with our simulation is shown in Figure 3 (right). Also, we have illustrated the principal shape of the rising bubble swarm in Figure 3 (left). In this snapshot we have colored the bubbles according to their absolute velocity in the bubble column.

The gassing rate is such that the total gas hold-up is in the range of 0.25–0.35 %, i.e., very low. To obtain time-averaged data, we have averaged the simulation output over a sufficiently long time (>100 s) to ensure that transient effects are excluded.

Unsteady Fluid Motion in the Bubble Column. It is well known, that even in the relatively simple setup considered in this work, i.e., the Becker case, the multiphase flow is unsteady and shows rich dynamic features. The correct prediction of the unsteady motion of the gas bubbles and the liquid phase is essential for a correct prediction of mixing. In order to verify our approach, we have focused on the time profile of the vertical component (i.e., along the z-direction) of the liquid-phase velocity at two distinct points in the bubble column. These two points are located in the upflow region, where a relatively high-gas holdup exists (Point A in Figure 3b), as well as in the downflow region, which is essentially free of bubbles (Point B in Figure 3b). The time signals for point A, as well as the power spectrum (obtained by frequency analysis using the fast Fourier transformation (FFT)) of the u_z-velocity in point A and B are shown in Figure 4 for two different meshes (mesh 0:64 × 10 × 192 = 122,880 cells; mesh 1:83 × 13 × 250 = 269,750 cells). Clearly, the time profiles (Figure 4a) for both meshes indicate similar features, i.e., a low-frequency oscillating motion, as well as superimposed high-frequency fluctuations. In our work, the minimum (filtered) velocities at point A was calculated as −0.39 and −0.30 m/s for the coarse and fine mesh, respectively. Whereas the peak velocity at point A are both 0.51 m/s for the coarse and fine grid. These features agree very well with the LDA measurements of Sokolichin and Eigenberger[87] (their minimum and maximum velocities were −0.4 and 0.8 m/s, respectively), as well as the simulations of Hu and Celik[39] (their minimum and maximum velocities were −0.3 and 0.5 m/s, respectively). A quantitative comparison of the oscillating motion is possible when looking at the results of the frequency analysis shown in Figure 4b. In point A the dominating oscillation period (indicated by the highest peak in the power spectrum) is equal to 41 s and 55 s for the coarse and the fine mesh, respectively. The oscillation period t_{osc} in point B is identical for both grids and equal to 41 s. Both values agree exceptionally well with literature data (Hu and Celik[39] and Becker et al.[68] reported an oscillation period of 41 s).

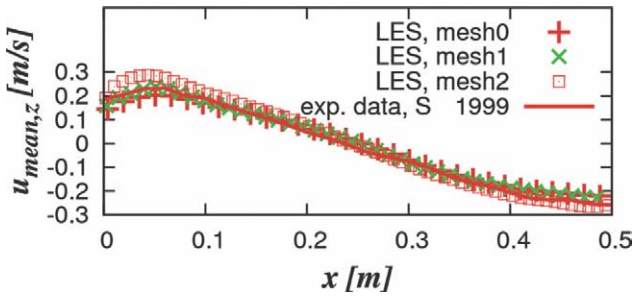

Figure 5. Comparison of the mean vertical velocity profiles at $z/H = 0.35$ for three different grids.

The data shown for mesh 0 and mesh 1 has been averaged over more than 100 s, data for Mesh 2 over 61.4 s. [Color figure can be viewed in the online issue, which is available at wileyonlinelibrary.com.]

Grid Refinement Study. In order to validate the results of our LES/Euler-Lagrange simulations, we performed a grid sensitivity study and compared the results to experimental data (from Sokolichin and Eigenberger[87]). We quantitatively compared the mean vertical velocity profiles at a relative height of z/h = 0.35 for three different mesh configurations (mesh 0:64 × 10 × 192 = 122,880 cells; mesh 1:83 × 13 × 250 = 269,750 cells; mesh 2:120 × 19 × 360 = 820,800 cells). All meshes are uniform, i.e., locally unrefined, and consisted of hexaeders. As can be seen from Figure 5, all grids gave excellent agreement with the experimental data. The mean-squared velocity differences (i.e., $1/N \cdot \Sigma(u_{mean,z,sim} - u_{mean,z,exp})^2$, where N is the total number of points used for comparison, and $u_{mean,z,sim}$ and $u_{mean,z,exp}$ are the simulated and experimentally measured z-velocity at the same location, respectively) obtained with the different meshes are summarized in Table 3. Mesh 1 was more accurate, whereas mesh 2 gave significant overprediction of in the region on the left-side of the column. It is speculated that this overprediction is due to the insufficient time-averaging performed for mesh 2, which was due to restriction in computational time. Thus, we conclude that even with the coarsest grid the unsteady motion of big turbulent eddies is captured accurately enough. Hence, we have chosen the coarsest grid, i.e., mesh 0 for all subsequent simulations.

Sensitivity to the Subgrid-Scale Model. Furthermore, we studied the influence of the subgrid-scale model on the results for the mean flow field and the subgrid-scale viscosity in the bubble column. The simulation included cases with (a) no subgrid-scale model, (b) the Smagorinsky model with $C_s = 0.032$ as suggested by Hu and Celik,[39] (c) the standard Smagorinsky model with $C_s = 0.16$, as well as (d) a differential one-equation model with standard coefficients ($C_k = 0.07$ and $C_\varepsilon = 1.05$). The reason for selecting the latter model is the suggestion of deVilliers.[63] He stated that more sophisticated dynamic models (which are not used in this work) become quite inaccurate in cases with poorly resolved wall regions. In contrast, the differential one-equation model is a good compromise between accuracy and computational resources needed.

The results for these four subgrid-scale models are depicted in Figure 6, and the results for the quantitative comparison are summarized in Table 3. Clearly, the Smagorinsky model with a low constant of $C_s = 0.032$ gives by far the best prediction of the mean flow field. The dynamic model (Figure 6d) has no significant advantages over the Smagorinsky model (Figure 6c), although it is computationally more expensive. Both models with standard coefficients strongly overpredict the subgrid-scale viscosity (compare the scales for the SGS viscosities in Figure 6). As expected, the simulation with the subgrid-scale model switched off (Figure 6a) overpredicts the mean flow field due to the absence of subgrid-scale energy dissipation. However, the overprediction is much weaker than the significant underprediction resulting from the standard SGS models. When looking at the predicted subgrid-scale viscosity values (Figure 6, right), the best model (i.e., the Smagorinsky model with $C_s = 0.032$) shows SGS viscosity values in the order of the molecular viscosity. This substantiates once more that the effect of the SGS velocity fluctuations on the mean flow field are rather small. However, the absence of the SGS model led to a too high-oscillation period (i.e., ca. 70 s for the SGS model switched off, vs. 41 s when the Smagorinsky model is activated) compared with experimental data. Hence, it is clear that for the multiphase simulations performed in this work (1) the Smagorinsky model together with the wall function approach of deVillier[63] is best suited for describing the subgrid-scale fluctuations, and (2) the standard value of C_s typically used for single-phase simulations is too high for multiphase flow simulations. Consequently, we have performed all following studies using the Smagorinsky model with $C_s = 0.032$. The underlying physical explanation for this very small Smagorinsky constant is most likely connected to the dissipation of turbulent kinetic energy by the gas bubbles. Thus, we assume that velocity fluctuations in the liquid phase are dampened out by the deforming gas-liquid interphase. This leads to a reduced amount of small-scale velocity fluctuations, which is not accounted for in the computer model used in our work. Similar speculations can be found in the PhD thesis of Hu.[89] Clearly, a more detailed analysis of this effects require future work in this area.

Sensitivity to the Mapping Scheme. In order to test the effect of the implemented mapping scheme, we have analyzed the oscillations that occur in the liquid-phase velocity field when performing the full two-way coupling between gas and liquid phase. These oscillations have been reported also by other researchers.[27] As a test case, an air bubble ($d_p = 0.010$ m) is tracked in a quiescent liquid (water). During the simulation the liquid-phase velocity at the bubble's position was recorded, and, subsequently, plotted vs. the vertical bubble position. The grid consisted of a rectangular box with the dimension $5 \cdot d_p \times 5 \cdot d_p \times 10 \cdot d_p$, and had a grid spacing of $1 \cdot d_p$. The results of this analysis are shown in Figure 7. As can be seen, the oscillations have a wave length equal to

Table 3. Mean-Squared Velocity Differences for the Grid Sensitivity Study, as well as for the Sensitivity to the Subgrid-Scale Model

Simulation Case	Mean Squared Velocity Difference
mesh 0	$4.9 \cdot 10^{-4}$ [m^2/s^2]
mesh 1	$2.3 \cdot 10^{-4}$ [m^2/s^2]
mesh 2	$6.9 \cdot 10^{-4}$ [m^2/s^2]
mesh 0, no SGS Model	$16.4 \cdot 10^{-4}$ [m^2/s^2]
mesh 0, $C_s = 0.16$	$52.9 \cdot 10^{-4}$ [m^2/s^2]
mesh 0, One-Eqn. SGS Model	$39.0 \cdot 10^{-4}$ [m^2/s^2]

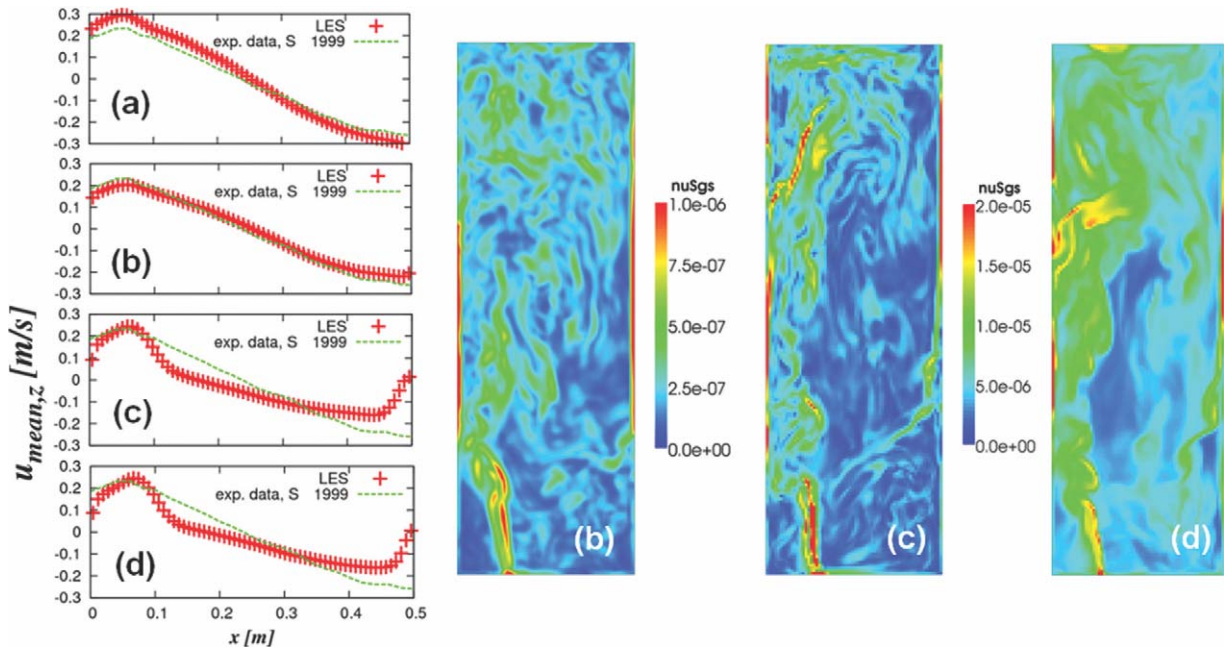

Figure 6. Comparison of the mean vertical velocity profiles at $z/H = 0.35$ (left), and snapshots of the subgrid-scale viscosity for three different subgrid-scale models (right; (a) no SGS model, (b) Smagorinsky model with $C_s = 0.032$ according to Hu and Celik, (c) standard Smagorinsky model with $C_s = 0.16$, and (d) differential SGS model; c and d share the same color bar for the subgrid-scale viscosity given in m^2/s).

[Color figure can be viewed in the online issue, which is available at wileyonlinelibrary.com.]

the grid spacing. To investigate this effect in more detail, we have analyzed the Euler-to-Lagrangian mapping scheme which performs the interpolation of Eulerian quantities at discrete locations (Figure 7, top). When this mapping is performed with the aforementioned advanced method, i.e., calculation via the virtual overlapping volumes (green dashed line in Figure 7, top), the oscillations of the liquid-phase velocity can be reduced significantly. Furthermore, we have analyzed how different settings of the Lagrangian-to-Euler mapping influence the oscillations (Figure 7, bottom). We present here some results connected to the overlap calculation scheme described earlier. The red continuous line (Figure 7 bottom, labeled "no skip") corresponds to a setting where all cells in the vicinity of the bubble's position for the overlap calculation are considered. This is computationally very expensive. The other curves correspond to settings for which cells are skipped that are out of the range of the bubble. This check was performed for three different values of $x_{cell,max}$ in Eq. 21. The value was increased linearly from setting 1 to setting 3. Clearly, when a too low value of $x_{cell,max}$ was selected, the total liquid velocity was (1) higher, and (2) the liquid-phase velocity fluctuations were significantly larger. Therefore, we used setting 3 in all following simulations. This setting required about 20% of the simulation time compared to the case in which the virtual overlapping volumes were calculated for all cell in the vicinity of the bubble's position (setting "no skip").

Mixing and reactions

Mixing in the liquid phase of a bubble column was studied by analyzing the filtered concentration distribution $\overline{Y}_i$ of an inert or reactive scalar. The filtered concentration distribution was obtained from the species transport equation (Eq. 15) after the flow field in the bubble column had already reached a quasi-steady state. This was the case after approximately 100 s. To analyze mixing, we either (1) set an initial distribution of a scalar quantity in the liquid phase, i.e., mixing without mass transfer, or (2) switched on mass transfer from the bubbles, i.e., mixing with simultaneous mass transfer.

Definition of Mixing Metrics. In order to quantify mixing, we define two metrics that characterize the intensity, as well as the scale of segregation. The intensity of segregation is

$$\sigma^2 = \frac{1}{\varepsilon_{L,mean} \cdot V_{tot}} \cdot \int_{V_{tot}} (\bar{Y}_i - \bar{Y}_{i,mean})^2 \cdot \varepsilon_L dV \qquad (35)$$

To characterize the scale of segregation (initially introduced by Bothe et al.[90]) we define the quantity

$$\Phi = \frac{1}{\varepsilon_{L,mean} \cdot V_{tot}} \cdot \int_{V_{tot}} |\nabla \bar{Y}_i| \cdot \varepsilon_L dV \qquad (36)$$

Φ is a metric for the mean driving force for mixing in the liquid phase and has been previously used to investigate mixing in microreactors.[90–92] In Eqs. 34 and 35, $\overline{Y}_{i,mean}$ is the mean concentration of species i in the bubble column, and V_{tot} is the total volume of the bubble column. ε_L is the local liquid-phase volume fraction. We have also analyzed the local distribution of these metrics by plotting the quantities $m_{\sigma^2} = (\overline{Y}_i - \overline{Y}_{i,mean})^2$, as well as $m_\Phi = \nabla \overline{Y}_i$.

Typical snapshots of these quantities are shown in Figure 8 (the base case as detailed in Table 2 using "mesh 0" is

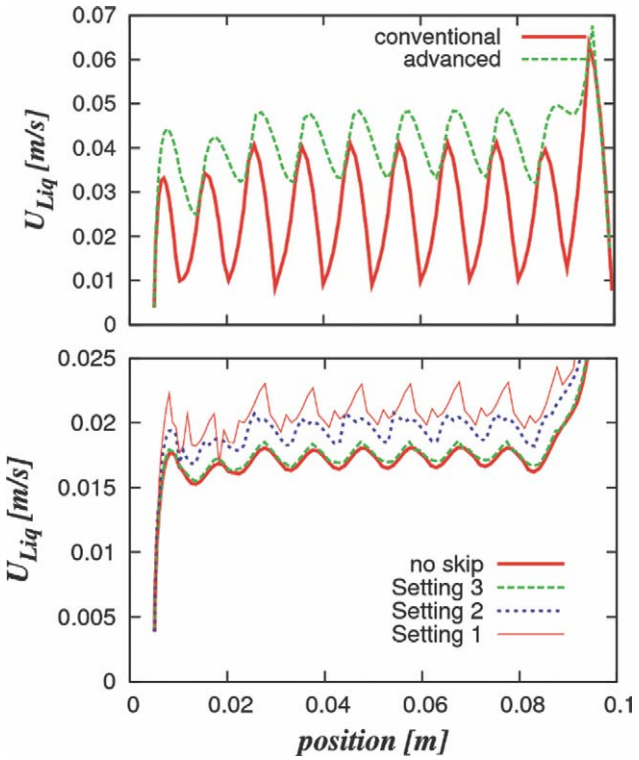

Figure 7. Comparison of different mapping schemes for the liquid-phase velocity at the bubble's center position (top: comparison of the Euler-to-Lagrangian mapping, bottom: comparison of different settings for the calculation of the virtual overlapping volume).

[Color figure can be viewed in the online issue, which is available at wileyonlinelibrary.com.]

shown). In Figure 8a the concentration has been made dimensionless using the equilibrium concentration at the gas-liquid interface. As can be seen from Figure 8a mass transfer from the gas to the liquid phase is slow and after 15 s the maximum concentration level is only about 4%. Furthermore, due to the inhomogeneous distribution of the gas bubbles in the bubble column, there exist regions that are totally void of dissolving gas. From Figure 8b it can be seen, that the intensity of segregation is initially small (Figure 8b, left), and increases at locations with high-mass-transfer rates and poor agitation by bubbles, e.g., at the top where the bubble plume becomes more widespread. Furthermore, the local distribution of σ^2 (Figure 8b) indicates high values at the lower right corner. In this area the transport of dissolved species is slowest. This is due to the large-scale circulation pattern in the bubble column. Figure 8c is a plot of Φ, i.e., it shows where local mixing occurs and how this area changes over time. Clearly, there is a strong driving force for mixing in the vicinity of the bubble swarm. However, as can be seen from Figure 8c (right), significant gradients in the concentration field are also present away from the bubble plume (bottom right corner).

To complete our understanding of mixing, we have also analyzed the volume distribution of m_{σ^2} and m_Φ. Thus, we have calculated the cumulative volume distributions $Q_3(m_{\sigma^2})$ and $Q_3(m_\Phi)$, as well as the corresponding volumetric frequency distributions $q_3(m_{\sigma^2})$ and $q_3(m_\Phi)$. This analysis was performed class-wise, i.e., we have defined 30 classes (defined by an upper and lower limit) ranging from zero to the maximum values of m_{σ^2}, as well as m_Φ. For the distribution functions of the intensity of segregation this can be formally written as

$$Q_3(m_{\sigma_u^2,i}) = \frac{1}{\varepsilon_{\mathrm{L,mean}} \cdot V_{\mathrm{tot}}} \cdot \sum_{V_{\mathrm{tot}}} H(m_{\sigma_u^2,i} - m_{\sigma^2,j}) \cdot \varepsilon_{\mathrm{L}} \cdot \Delta V_j \quad (37)$$

$$q_3(m_{\sigma_m^2,i}) = \frac{\Delta Q_3(m_{\sigma_m^2,i})}{\Delta m_{\sigma_m^2,i}} = \frac{Q_3(m_{\sigma_u^2,i}) - Q_3(m_{\sigma_u^2,i-1})}{m_{\sigma_u^2,i} - m_{\sigma_u^2,i-1}} \quad (38)$$

Here, $H()$ is the heaviside function. The indices i and j indicate the class index and the volume element index, respectively. The upper limit of the class i is denoted by $m_{\sigma_u^2,i}$, and the mean of class i by $m_{\sigma_m^2,i}$. For the distribution of m_Φ similar expressions can be derived. By analyzing these two distributions it is possible to characterize the

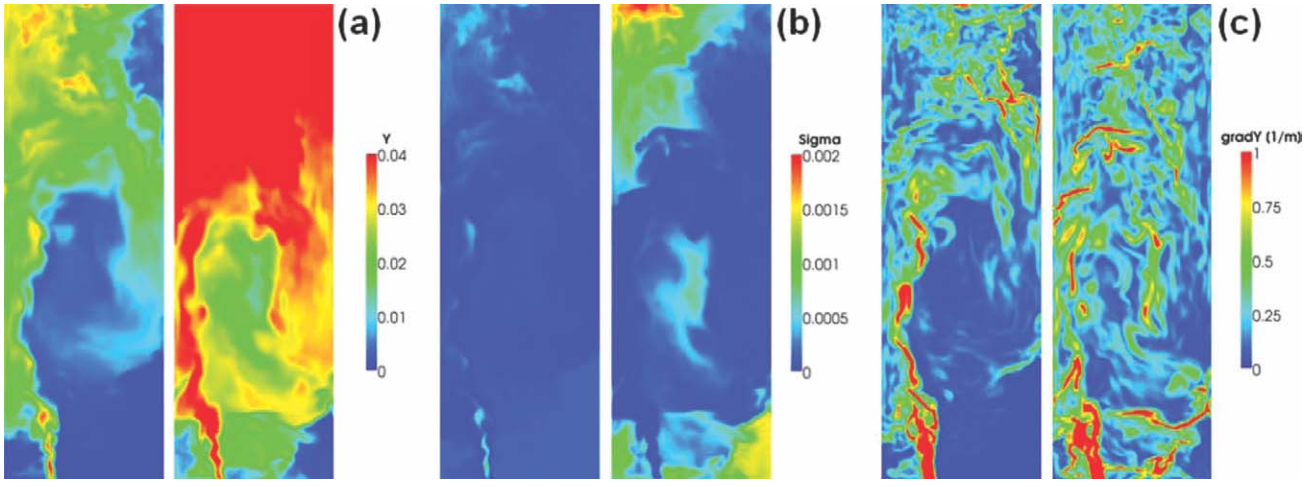

Figure 8. Contour plots of (a) concentration field Y, (b) local distribution of the intensity of segregation σ^2, and (c) scale of segregation Φ (left: t = 5 s, right: t = 15 s).

[Color figure can be viewed in the online issue, which is available at wileyonlinelibrary.com.]

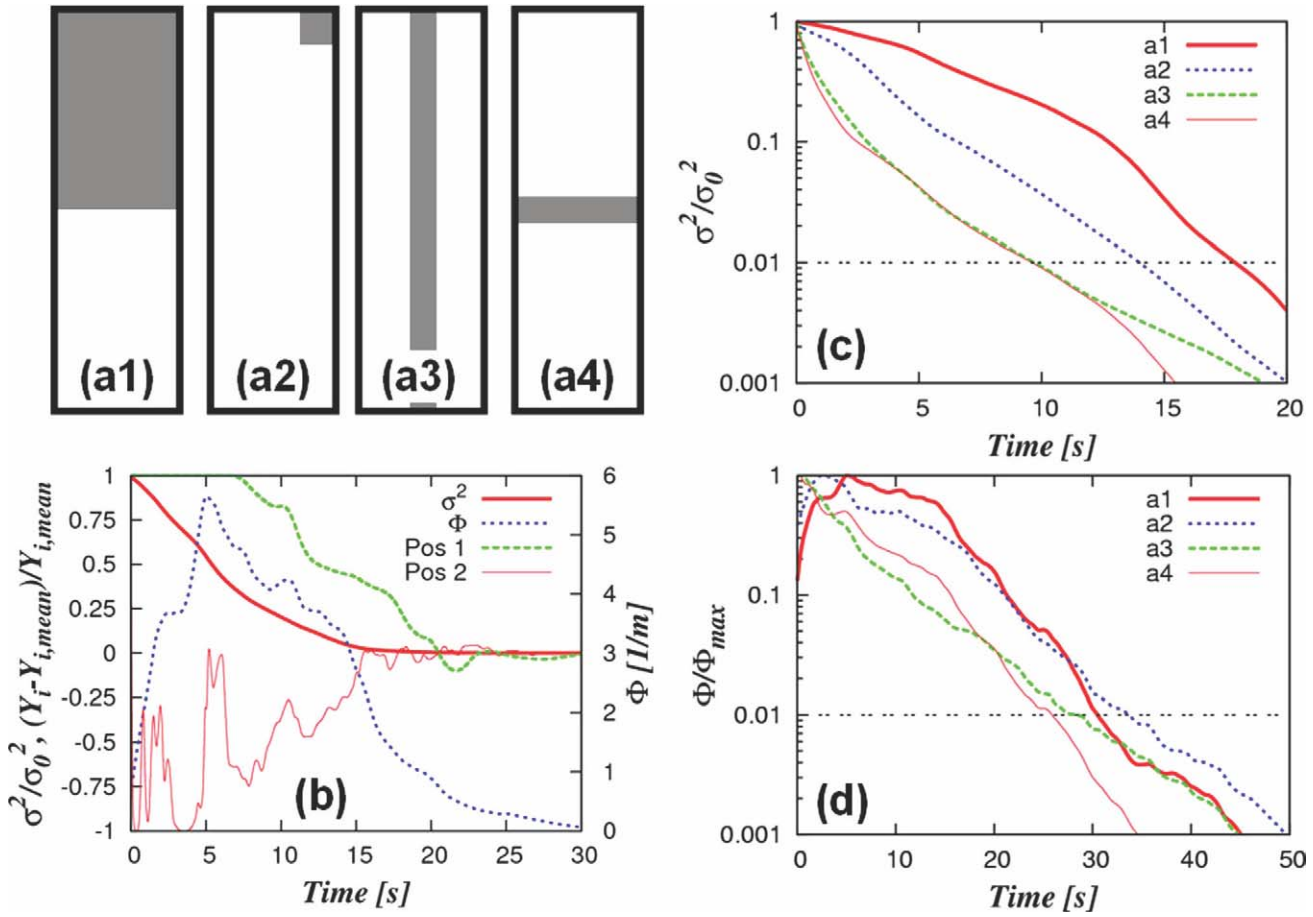

Figure 9. Analysis of mixing metrics for different initial distributions of an inert scalar without mass transfer (a1: "half-half" distribution; a2: "corner" distribution; a3: "vertical" distribution; a4: "horizontal" distribution; b: mixing metrics for the half-half initial distribution, Pos 1: x =0.001, y =0.001, z = 0.001, Pos 2: x = 0.250, y = 0.040, z = 0.750; c: normalized intensity of segregation vs. time; d: normalized scale of segregation vs. time).

[Color figure can be viewed in the online issue, which is available at wileyonlinelibrary.com.]

homogeneity of mixing in the reactor. To facilitate such an analysis, we have fitted the frequency distribution of m_Φ with a logarithmic normal distribution of the form

$$q_{3,LN}(x) = \frac{1}{\sqrt{2\pi}\cdot\sigma\cdot x}\cdot\exp\left[-\frac{\left\{\ln\left(\frac{x}{\mu}\right)\right\}^2}{2\cdot\sigma^2}\right] \tag{39}$$

Here, σ is the standard deviation, and μ (1/m) is the mean of the distribution.

Scalar Mixing without Mass Transfer. In order to analyze the liquid-phase mixing of an inert scalar in the bubble column without mass transfer we simply switched off mass transfer. In addition, these simulations were used to check the accuracy of the developed method with respect to the conservation of scalars, i.e., we monitored the total mass of the scalar during the simulation. This conservation check showed that the used numerical schemes and the settings of the solver led to a conservation of the total mass of the inert scalar within ±0.2% for a total simulation time of 100 s.

The initial distributions of the inert scalar are shown in Figure 9a1 to Figure 9a4. First, we analyzed which mixing metric is the most suitable one to be used for our studies. Therefore, the scale and intensity of segregation are plotted together with the normalized concentrations at two different positions (see Figure 9b, Pos 1 refers to a position in the corner of the bubble column, whereas Pos 2 is located in the center of the bubble column). For this study the "half-half" initial distribution was used (Figure 9a1). As can be seen clearly from Figure 9b the time profiles of the normalized concentration distributions give a highly noisy signal. The plots indicate that complete mixing is obtained after approximately 18 and 25 s for Pos 2 and Pos 1, respectively. In contrast, the time profiles in Figure 9b for the normalized intensity and scale of segregation show a smooth profile. This is because they represent an integral measure for mixing, and, hence, better represent the total state of the bubble column. In addition, these curves show characteristic points, i.e., the scale of segregation has a pronounced peak after approximately 5 s and then shows a steady decrease. This peak can be interpreted as the time when the maximum driving force is present in the system, i.e., where mixing is fastest. In conclusion, the mixing metrics σ^2 and Φ seem to be better suited to define mixing time scales than concentration profiles, as the latter are

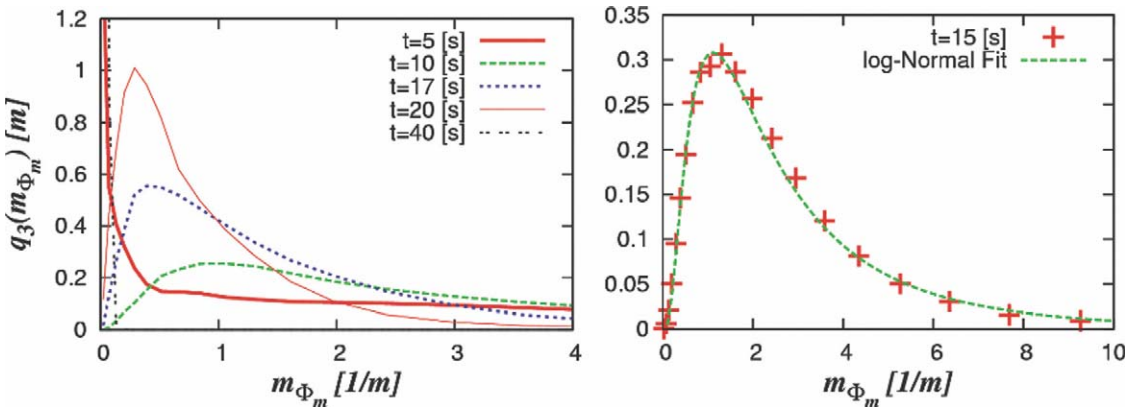

Figure 10. Distribution of the scale of segregation for an inert scalar without mass transfer (initial distribution according to Figure 9a1; left: comparison of distributions for different times, right: lognormal fit of the distribution after a time of 15 s).

[Color figure can be viewed in the online issue, which is available at wileyonlinelibrary.com.]

sensitive to local velocity fluctuations and the absolute position in the reactor.

Second, we analyzed the effect of the initial distribution of the inert scalar on the mixing metrics of interest (Figure 9c and 9d). As can be seen from these graphs, the normalized intensity of segregation (the initial value of σ^2 was used as the reference) shows large differences in the time profiles for different initial distributions and predicts characteristic mixing times between 9 and 17 s (deviation of ± 31 %, we have taken $\sigma^2/\sigma_0{}^2 = 0.01$ as "perfectly mixed"). In contrast, the normalized scale of segregation is much less sensitive to the initial distribution of the scalar and gives significantly higher mixing times between about 27 and 34 s (deviation of ± 11 %, we have taken $\Phi/\Phi_{max} = 0.01$ as "perfectly mixed"). In conclusion, the scale of segregation, representing the driving force for mixing, seems to be the most appropriate metric for investigating mixing times.

In Figure 10 we have analyzed the frequency distribution of the scale of segregation for the case of the "half-half" distribution of the inert scalar. For time zero, the distribution of the scale of segregation has two peaks: (1) at zero (corresponding to the zone where the concentration is uniform), and at (2) infinity (corresponding to the interface between the region with and without inert scalar) Clearly, for the shortest time (see Figure 10, left) the peak near zero is still present, whereas for higher values of the scale of segregation the curve is monotonically decreasing. After approximately 10 s, zones of uniform concentration have completely vanished. This is indicated by the fact that the distribution now has a value of zero at the origin. As mixing goes on, the distribution becomes narrower and the peak is moving to a smaller value of m_{Φ_m}. Thus, the concentration field becomes more uniform and the driving force for mixing is decreasing. Interestingly, also the driving force becomes more uniformly distributed as indicated by the narrower distribution at later times.

In Figure 10 (right), we show the fit of the distribution of the scale of segregation after 15 s. Clearly, the correspondence between simulation results and the fitting function (Eq. 38) is nearly perfect indicated by a root-mean-square value of residuals for this fit of 0.00942. A detailed analysis of this surprising finding was not performed in our work. However, it strongly suggests that the distribution of

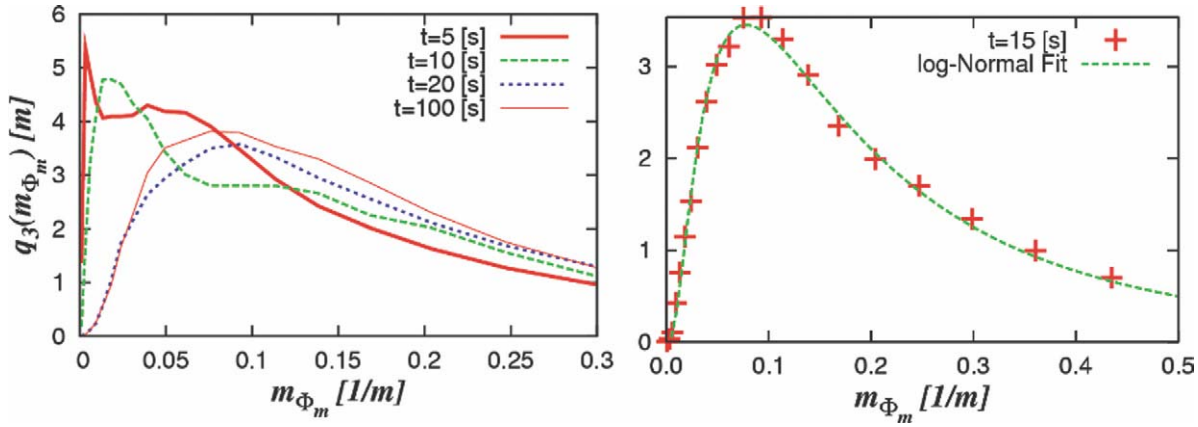

Figure 11. Distribution of the scale of segregation for the base case with mass transfer (d_p = 1.6 mm, V_G = 1.6L/min, mesh 0) (left: comparison of distributions for different times, right: log-normal fit of the distribution after a time of 15 s).

[Color figure can be viewed in the online issue, which is available at wileyonlinelibrary.com.]

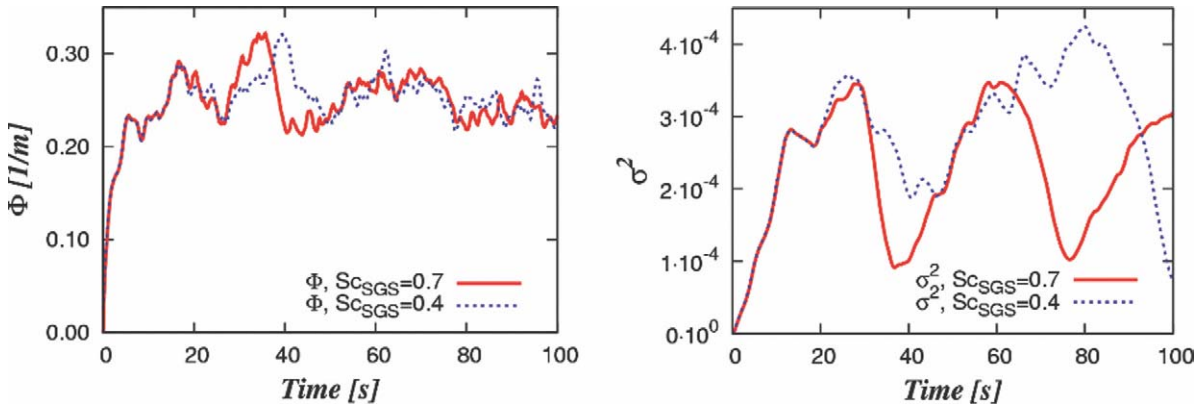

Figure 12. Mixing metrics for different subgrid-scale Schmidt numbers Sc_{SGS} (left: scale of segregation, right: intensity of segregation).

[Color figure can be viewed in the online issue, which is available at wileyonlinelibrary.com.]

concentration gradients in bubble columns is possibly caused by a simple mechanism, e.g., stretching and folding of fluid elements similar to single-phase flow.

Scalar Mixing with Mass Transfer — Distribution of the Scale of Segregation. In Figure 11 we illustrate the distribution of the scale of segregation for the base case with mass transfer (d_p = 1.6 mm, and V_G = 1.6 L/min). Similar to the case without mass transfer the distribution becomes almost perfectly log-normal after a certain time (see Figure 11, right). However, in contrast to the case without mass transfer, initially no peak at $m_{\Phi_m} = \infty$ is present. Furthermore, the slow mass transfer from the gas- to the liquid phase leads to areas having a small scale of segregation (see Figure 11 left, peak in the curve for t = 10 s).

Mixing with Mass Transfer — Basic Observations and Impact of Sc_{SGS} on the Mixing Metrics. Before analyzing the mixing in the system including mass transfer, the effect of different values of the subgrid-scale Schmidt number Sc_{SGS} on the mixing metrics was quantified. Figure 12 shows the dependency of the two mixing metrics σ^2 and Φ vs. time for two different values of Sc_{SGS}. For this analysis we set the equilibrium concentration at the gas-liquid interface equal to one, i.e., the following results are also applicable to concentration fields normalized with the equilibrium concentration.

As can be seen in Figure 12, the characteristics of the time profiles of both mixing metrics are substantially different from the case without mass transfer (Figure 9c–d). First, the scale of segregation seems to reach a plateau value after an initial increase. This means that a slightly fluctuating, nearly constant driving force for mixing is established rapidly in the bubble column. Second, the intensity of segregation fluctuates significantly stronger and the fluctuations show a characteristic frequency of approximately 40 s. This characteristic frequency corresponds to the fluctuation of the gas holdup (see Figure 16c, curve for d_p = 1.6 mm). Thus, when the gas holdup decreases also the intensity of segregation decreases. This effect is caused by two phenomena: first, due to the decreased rate of mass transfer at a lower gas holdup, the local concentration fluctuations in the bubble column also become smaller. Second, the instantaneous

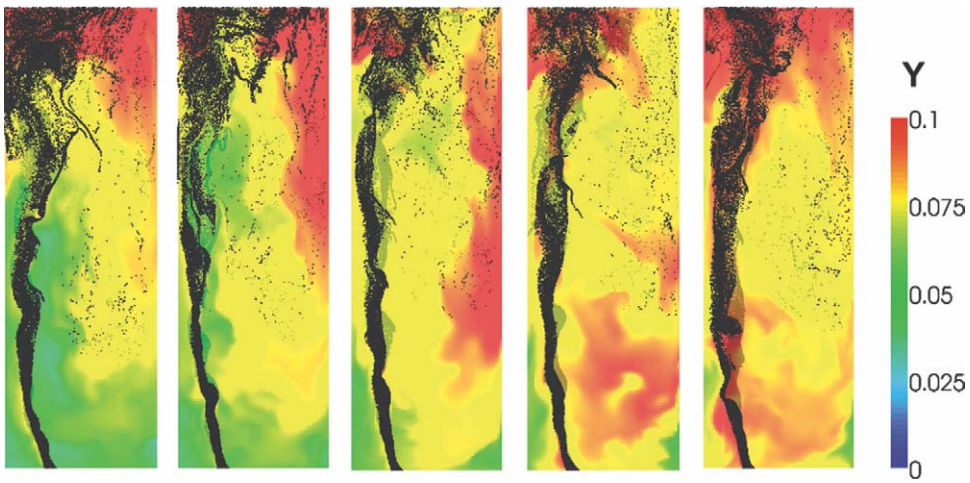

Figure 13. Concentration contour plot and bubble positions for Sc_{SGS} = 0.7 (images correspond to snapshots at t = 30 s, t = 32 s, t = 34 s, t = 36 s, and t = 38 s from left to right, the concentration field has been made dimensionless using the equilibrium concentration at the gas-liquid interface).

[Color figure can be viewed in the online issue, which is available at wileyonlinelibrary.com.]

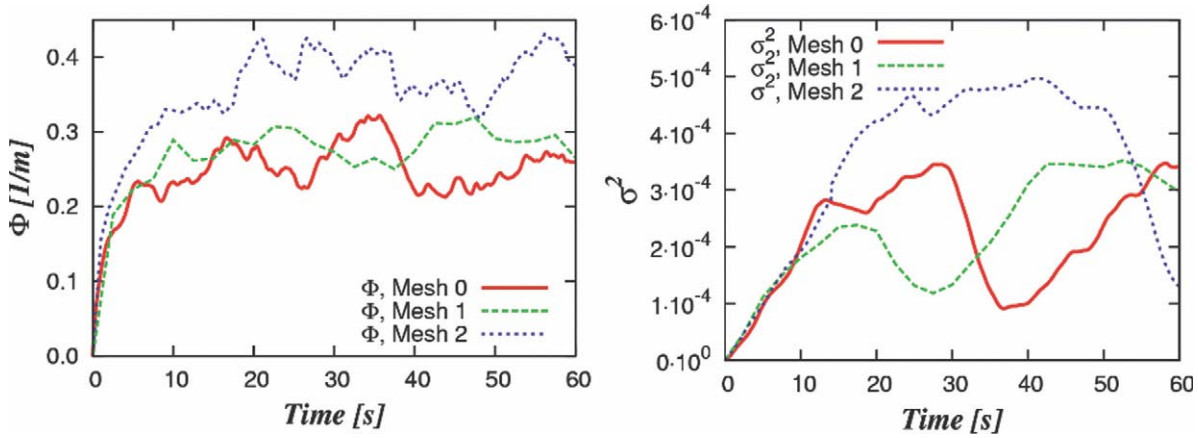

Figure 14. Grid sensitivity study of mixing metrics (left: scale of segregation, right: intensity of segregation).

[Color figure can be viewed in the online issue, which is available at wileyonlinelibrary.com.]

mixing rate is only weakly influenced by the gas holdup. This is due to the slowly decaying liquid-phase turbulent motion in the liquid phase. Both phenomena lead to a strong increase in the intensity of segregation as the quadratic deviations from the mean concentration are used for the calculation of σ^2 (see Eq. 34). To illustrate this effect, dimensionless concentration contour plots for different times between $t = 30$ s and t = 38 s are shown in Figure 13. Clearly, at t = 30 s a cloud of high concentration has formed at the top section of the bubble column. At this moment, due to fluctuations in the liquid-phase velocity field, the gas holdup starts to decrease (see Figure 16c). Subsequently, the cloud is transported downward by the main recirculation loop and mixed with the liquid in the lower right corner of the bubble column (see Figure 13, images for $t = 32$ s to $t = 38$ s). When comparing this behavior for different Sc_{SGS} (see Figure 12), we observe that the magnitudes of both mixing metrics are very similar in both cases. Therefore, we conclude that the subgrid-scale Schmidt number does not have a significant impact on mixing. Hence, we used the value of $Sc_{SG}S = 0.7$ for all following computations in our work.

Impact of Grid Size on the Mixing Metrics. Same as for the liquid-phase flow, we have performed a grid-sensitivity analysis of the results for the mixing metrics. Again, we have set the equilibrium concentration at the gas-liquid interface equal to 1.

As can be seen from Figure 14, with the medium and fine grid more details of the concentration field can be resolved, and, hence, a larger scale of segregation Φ is obtained. In addition, it is clear that numerical diffusion decreases with increasing mesh resolution resulting in a higher accuracy with respect to the resolution of the concentration field. However, as we have used identical numerical schemes throughout this work, the effect of numerical diffusion is identical for all simulation cases.

For the intensity of segregation (refer to the trend of $\sigma^2_{\text{av,0–100 s}}$ in Table 4) a similar trend is observed. However, the strong fluctuation in this mixing metric prohibits a direct comparison of the curves for different grids. This effect is due to the sensitivity of σ^2 to the local flow field, i.e., the grid resolution affects the flow field, and, consequently, the gas holdup, as well as the local concentration distribution.

In conclusion, also the coarsest grid gives satisfactory resolution of the concentration field, and it is supposed that trends for mixing are well captured with this grid.

In Table 4 we show the influence of a finer grid spacing on the time-averaged mean gas holdup and different metrics for mixing. First, the differences in the calculated gas holdups averaged over 100 s, i.e., $\varepsilon_{\text{G,mean,0–100 s}}$, are small and are well below 10%. Thus, the grids give essentially the same results for multiphase flow. Second, the mixing metric Φ_{av}, i.e., the scale of segregation, increases with increasing mesh resolution. Thus, spatial gradients in the concentration field are resolved better with smaller grid spacing. This gives a significantly higher value for Φ_{av} for the finest grid. This trend is also visible for the mean value of the distribution of m_Φ taken after 60 s. Similar to the scale of segregation, the intensity of segregation is highest for the finest grid. This is due to the fact that (1) the concentration field is better resolved with a finer grid, (2) numerical diffusion is reduced when using smaller grid spacing, and (3) the intensity of segregation is a function of the sample volume which corresponded to the volume of a computational cell, i.e., was much smaller for the finer grid. Third, the standard deviation of the distribution of the scale of segregation decreases with increasing grid resolution. This also reflects the higher spatial resolution of the concentration field, less numerical diffusion, and, hence, a narrower distribution in case of a smaller grid spacing.

In summary, while the hydrodynamics seem to be unaffected by the grid size, the trends in the calculated mixing metrics show a certain grid dependency. This grid dependency stems from (1) the high Schmidt numbers in the liquid phase leading to extremely fine concentration patterns that

Table 4. Grid Dependency of Gas Holdup and Mixing Metrics, $d_p = 1.6$ mm, $V_G = 1.6$ L/min (Time-Averaging was Performed for 60 s only for the Case Involving Mesh 2)

Parameter	Mesh 0	Mesh 1	Mesh 2
$\varepsilon_{\text{G,mean,0-100s}}$	0.187	0.181	0.202
$\Phi_{\text{av,0-100s}}$ [1/m]	0.247	0.253	0.378
$\sigma^2_{\text{av,0-100s}}$	$2.24 \cdot 10^{-4}$	$2.02 \cdot 10^{-4}$	$4.04 \cdot 10^{-4}$
$\mu_{m_\Phi,60s}$ [1/m]	0.192	0.185	0.271
$\sigma_{m_\Phi,60s}$	1.02	0.911	0.864
Δx [mm]	7.81	6.00	4.17

Table 5. Influence of Bubble Size (at V_G = 1.6 L/min) and Gas-Flow Rate (with d_p = 1.6 mm) on Gas Holdup, Interfacial Area and Mixing Metrics

Parameter	d_p = 1.6 [mm]	d_p = 2.4 [mm]	d_p = 3.2 [mm]	d_p = 4.8 [mm]	V_G = 0.4 [L/min]	V_G = 0.8 [L/min]	V_G = 3.2 [L/min]
ε_G	0.187	0.141	0.129	0.116	0.0523	0.0923	0.357
a [m^2/m^3]	7.00	3.52	2.42	1.45	1.96	3.46	13.4
$\mu_{m_\Phi,60s}$ [1/m]	0.192	0.127	0.0661	0.0467	0.109	0.132	0.154
$\sigma_{m_\Phi,60s}$	1.02	0.988	0.992	1.138	1.05	0.891	0.968

cannot be resolved with the current LES, and (2) the principal inability of LES to yield grid independent results.[93] Since it is clear that it will never be possible to fully resolve all details of the concentration field by using LES, it is essential to show and recognize the trends due to different grid sizes. Clearly, the observed trends for the mixing metrics over the grid size are consistent. Hence, at a fixed grid size it should be possible to compare simulation results for different operating conditions. Thus, we conclude that the used grid size (i.e., mesh 0) is suitable to study the influence of bubble size, gas-feed rate, domain size, as well as relatively slow chemical reactions (i.e., that are not influenced by subgrid-scale fluctuations) on the mixing conditions in the bubble column.

Long-Term Behavior of the Mixing Metrics. For the medium grid used in our work (mesh 1), we studied the long-term behavior of the mixing metrics. With long-term behavior we refer to the influence of the accumulated species that is transferred from the gas to the liquid phase. In Figure 15 we show the time profiles for σ^2 and Φ together with curves that are of the form

$$y(t) = y_0 \cdot \exp\left[-\frac{t}{\tau}\right], \tag{40}$$

where y is one of the two mixing metrics used, i.e., Φ or σ^2, y_0 is the mixing metric at time zero, and τ is the time constant for mass transfer, i.e., $1/(k_L{\cdot}a)$. Thus, Eq. 40 predicts the time evolution of the concentration difference between the equilibrium concentration at the interface (set equal to one in our simulations), and the mean concentration in the liquid phase (Eq. 40 can be derived from a simple mass balance of the dissolving species in the liquid phase). Note, that the average of $k_L{\cdot}a$ is known from the simulations, and that y_0 has been calculated by fitting $y(t)$ to the instantaneous values for σ^2 and Φ. As can be seen from Figure 15, the function given by Eq. 39 is able to approximate the decrease of both mixing metrics in time reasonably well. Thus, both mixing metrics depend linearly on the concentration difference between the gas-liquid interface and the mean bulk concentration. This result reflects the simple fact that the mixing metrics only depend on concentration differences and not on absolute values for the concentration.

Effect of the Bubble Size on Mixing. In the following, we analyzed the effect of the bubble size on the mixing in the bubble column. For this analysis we have included mass transfer from the gas phase to the liquid phase (equilibrium concentration set equal to 1), and have assumed zero initial concentration in the liquid phase. Also, we have kept the gas-feed rate constant, i.e., the total power input into the system is not increased (the total power input is the product of the gas-feed rate and the pressure difference between gas inlet and outlet). However, we expect the total mass-transfer rate to increase with decreasing bubble size and to get similar mixing rates in the system as the power input is identical. The driving force, i.e., the scale of segregation, should decrease with increasing bubble size because the total mass transferred into the liquid bulk becomes smaller.

The time profiles for these simulations are shown in Figure 16 and important results are summarized in Table 5. Clearly, the initial transient for Φ is similar, i.e., very fast, for all bubble diameters indicating similar mixing rates. However, the main difference is that, as expected, the scale of segregation (Figure 16a), as well as the intensity of segregation (Figure 16b) is smaller for the larger bubbles. In addition, the latter measure is fluctuating significantly more strongly for smaller bubbles. This is caused by the stronger fluctuations in the gas holdup resulting in a fluctuation of the specific interfacial area a (Figure 16c). Note, that the interfacial area was calculated directly from the mean gas holdup by $a = \varepsilon_G \cdot 6/d_p$. To quantify the effect of the specific interfacial area on Φ, we have calculated the dimensionless quantity Φ/a. As can be seen from Figure 16d, this quantity is similar for all cases studied. Thus, an important result of our work is that the scale of segregation is inversely proportional to the bubble diameter. Also, the intensity of segregation decreases with increasing bubble diameter, since the total amount of dissolved gas and consequently its mean concentration is lower due to the lower interfacial area of the larger bubbles. Again, as we see in the insert in Figure 16d (showing the first 10 s of the Φ/a time profile), the initial transient in Φ/a is similarly fast indicating similar mixing rates.

Effect of the Gas-Feed Rate on Mixing. As the power input is directly proportional to the gas-feed rate, an increase in the feed rate should lead to an increase of the mixing rate. In other words, the mesomixing time scale should

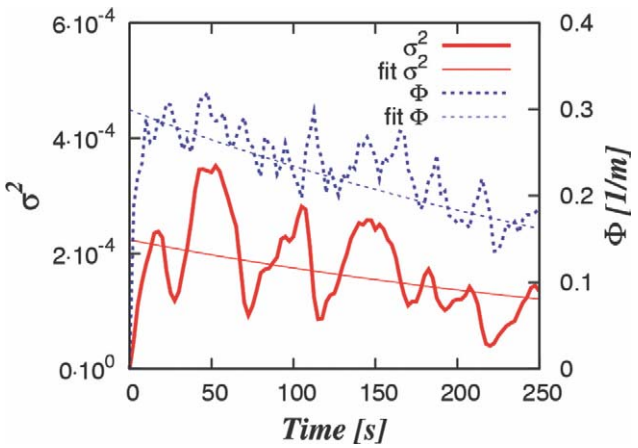

Figure 15. Time profiles for the mixing metrics σ^2 and Φ for long times (mesh 1).

[Color figure can be viewed in the online issue, which is available at wileyonlinelibrary.com.]

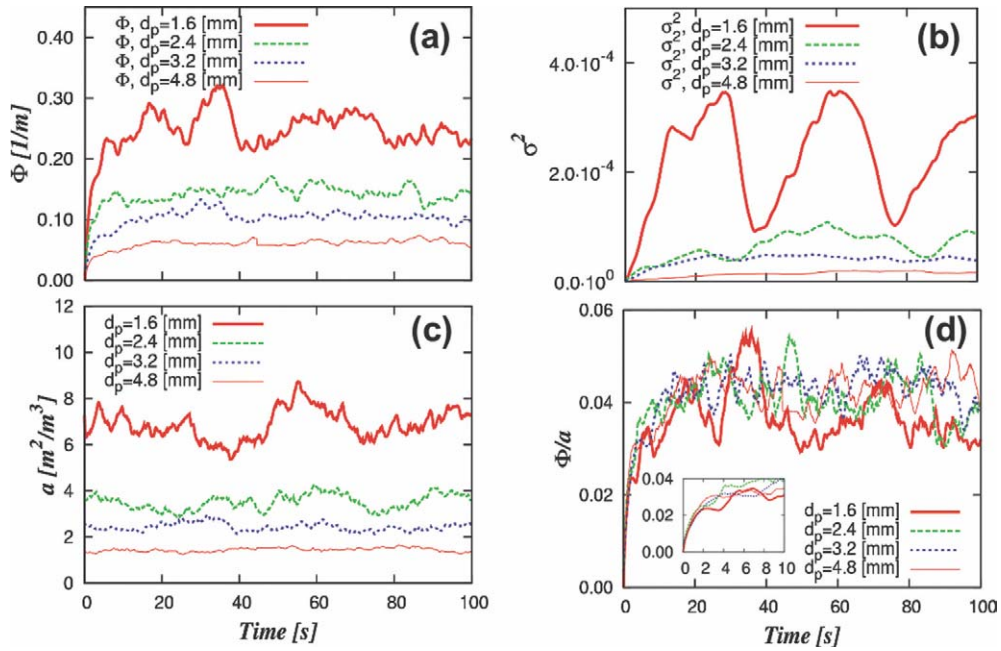

Figure 16. Time profiles of mixing metrics and interfacial area for different bubble sizes: (a) scale of segregation, (b) intensity of segregation, (c) interfacial area, and (d) ratio of scale of segregation and interfacial area.

[Color figure can be viewed in the online issue, which is available at wileyonlinelibrary.com.]

become smaller. Also, the gas holdup will increase with increasing gas-feed rate, leading to a higher rate of mass transfer, and, consequently, to an increase of the scale of segregation.

In Figure 17 the results are shown by plotting the two mixing metrics as a function of time. Important results for the effect of the gas-feed rate on mixing are summarized in Table 5. As expected, in the case of $V_G = 0.4$ L/min, we observe the slowest transient in σ^2 (Figure 17b). Also, a small increase in the scale of segregation is visible from our simulation results. This increase is, however, significantly less pronounced compared to the effect of the bubble size. This is due to the fact, that the increased mass transfer rate (see Figure 17c where we have plotted the specific interfacial area a) is counterbalanced by increased mixing for the

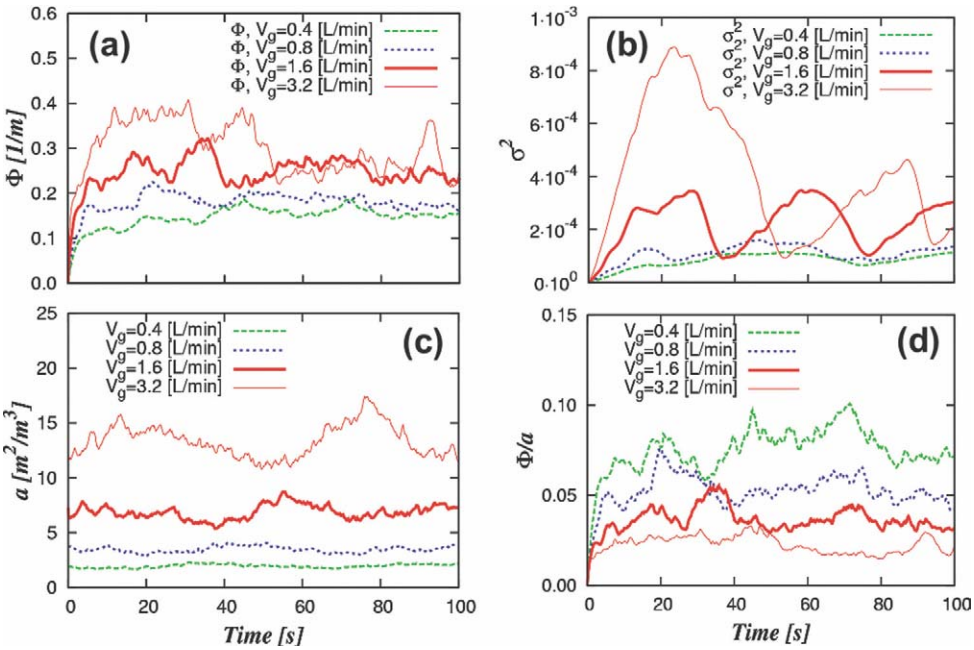

Figure 17. Time profiles of mixing metrics and interfacial area for different gas feed rates: (a) scale of segregation, (b) intensity of segregation, (c) interfacial area, and (d) ratio of scale of segregation and interfacial area.

[Color figure can be viewed in the online issue, which is available at wileyonlinelibrary.com.]

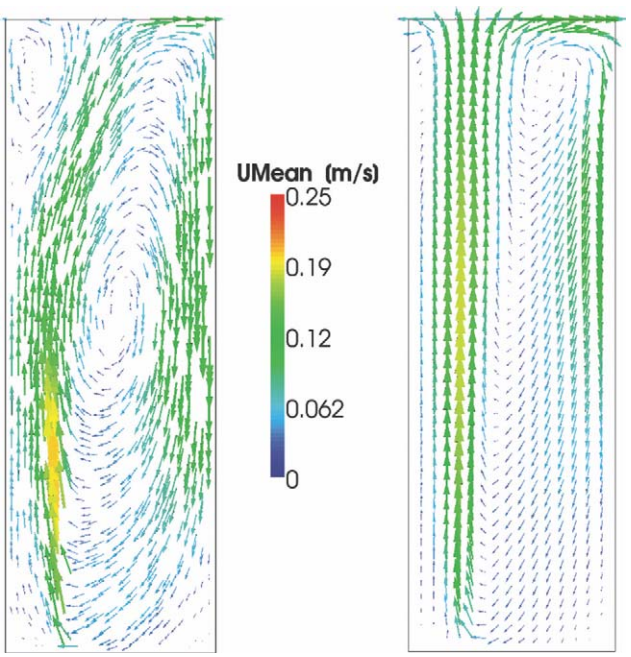

Figure 18. Time-averaged flow field for the bubble column with (left) one half, and (right) one quarter of the size as the base case (both figures share the same color scale).

[Color figure can be viewed in the online issue, which is available at wileyonlinelibrary.com.]

higher gas-feed rate. Consequently, if we try to make Φ dimensionless by division by a, we do not get similar dimensionless values for Φ/a for different gas-feed rates (see Figure 17d). In contrast, the case with the lowest gas-feed rate, i.e., $V_G = 0.4$ L/min gives the highest dimensionless value of Φ/a indicating the lowest mixing rate in the system.

Scale-Up: Effects of the Domain Size on Mixing. We also investigated the effect of the system size on the mixing properties, and, thus, performed two additional simulations with identical superficial gas velocity for different widths (dimension W in Figure 2) of the bubble column. The two simulations were performed with one-half and one-quarter of the width of the bubble column, i.e., with W = 0.25 m, and W = 0.125 m, respectively. We used identical grid spacing for all these simulations in order not to influence the mixing metrics. This is especially important with respect to the calculation of the scale of segregation Φ. Also, bubble size, height to width-ratio and the depth of the bubble column were held constant. We have kept the depth of the column constant in order to minimize effects stemming from different cell counts in y-direction.

In the simulations of the smaller bubble columns the mean gas holdup, and, consequently, the interfacial area were essentially the same as for the base case detailed in Table 2 (see Figure 3, ε_G was 0.196 and 0.204 for the case with one-half and one-quarter of the size, respectively). Also, the mean liquid-phase velocity distribution in the bubble column agreed well with that of the base case (see Figures 18 and 3b). However, the overall liquid-phase velocities were significantly smaller for the simulations with reduced size. For the quarter-sized column (Figure 18, right), the recirculation zone near the top disappeared, and the main circulation loop was significantly shifted upward. Surprisingly, the time profiles for the scale of segregation for different sizes of the computational domain compare reasonably well with each other (see Figure 19, left). As expected, the intensity of segregation (see Figure 19 right) is the highest and the frequency of the oscillation is the lowest for the full-scale bubble column. The significantly higher frequency in the oscillation of σ^2 for the smallest bubble column (Figure 19 right, $1/4$ size) is due to the fact that all bubbles rise almost vertically in this setup, i.e., there is no significant oscillation of the gas holdup (results not shown). Hence, it seems that the intensity of segregation does not only depend on the superficial gas velocity or the specific power input (note that the latter is also constant as the superficial gas velocity was held constant). Surprisingly, Φ is only weakly influenced by the scale (see Figure 19, left). This is an interesting finding, since it provides a basis for the scale-up of bubble columns with respect to mass transfer and mixing.

Mixing and Chemical Reactions in Fermentation Reactors. In the final part of our analysis the interaction of mesoscale mixing with a typical fermentation reaction was investigated. For this purpose we studied the oxygen uptake by microorganism suspended in the liquid phase of the bubble column. For typical conditions in an industrial fermenter, the oxygen saturation concentration $Y_{02,sat}$ in the liquid phase

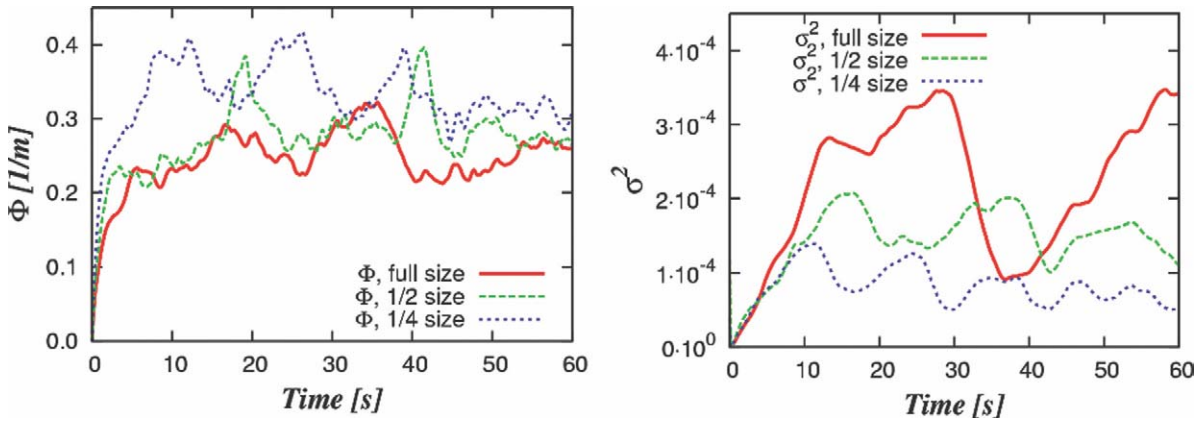

Figure 19. Effect of the size of the computational domain on the mixing metrics.

[Color figure can be viewed in the online issue, which is available at wileyonlinelibrary.com.]

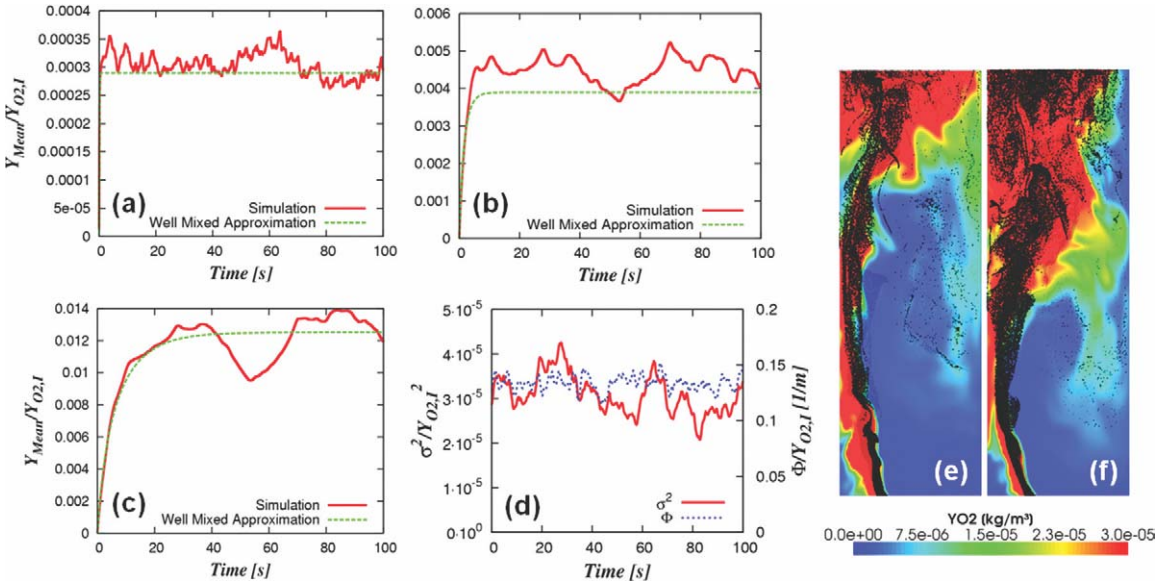

Figure 20. Dimensionless mean concentration profiles: (a) τ_R = 10 s, (b) τ_R =100 s, (c) τ_R = 200 s, (d) mixing metrics for the case with τ_R = 100 s; and snapshots of the concentration profile and bubbles for the case with τ_R = 100 s: (e) t = 52 s, and (f) t = 70 s.

[Color figure can be viewed in the online issue, which is available at wileyonlinelibrary.com.]

should be between 5 and 8 mg/L. The oxygen consumption in such a fermentation can become significant, such that mixing and mass transfer become rate limiting. Furthermore, it is well known that under non-ideal conditions, the microorganisms excrete byproducts, e.g., ethanol and glycerol,[94] leading to a reduction of the yield. Hence, a strategy to estimate mixing and mass transfer in these reactors would give better tools for an optimized design.

The kinetic expression for oxygen uptake by microorganisms in fermentations can be described by, e.g., a Michaelis-Menten-type rate equation

$$r_{O_2} = k_{0,0} \cdot \frac{Y_{O_2}}{K_O + Y_{O_2}} \tag{41}$$

Here r_{O2} is the oxygen uptake rate, $k_{0,0}$ is a reaction rate constant, Y_{O2} is the concentration of oxygen in the reactor and K_O is the Michaelis-Menten constant. K_O is typically small compared to the equilibrium concentration of oxygen in the liquid phase. Consequently, the oxygen uptake rate r_{O2} is nearly constant, i.e., we have an almost zero-order oxygen uptake in the fermenter. For the current analysis we have taken $Ko = 5 \cdot 10^{-5}\ kg/m^3$, which is typical for fermentations (e.g., refer to the analysis of Sweere et al.[94] for baker's yeast). K_O is two-orders of magnitude smaller compared to the oxygen saturation concentration $Y_{O_2,I} = Y_{O_2,sat} = 5{\cdot}10^{-3}\ kg/m^3$.

In our work we focus on relatively slow reaction kinetics and analyze the concentration distribution, as well as the interaction with mixing for characteristic reaction times τ_R ranging from 10 to 200 s. τ_R is defined as the ratio of the oxygen saturation concentration and the reaction rate constant, i.e., $\tau_R = Y_{O_2,I}/k_{0,0}$. Thus, compared to the mass-transfer time constant in the bubble column (which can be calculated from the inverse of the average value for $k_L{\cdot}a$, yielding approximately 400 s), the oxygen uptake by the microorganisms is faster. Furthermore, the micromixing time τ_M can be estimated using the engulfment model Eq. 42[95]

$$\tau_M = 17 \cdot \left(\frac{\nu}{\varepsilon}\right)^{1/2} \tag{42}$$

A micromixing time of approximately 0.2 s is obtained when assuming that the energy dissipation rate is uniformly distributed in the bubble column. Thus, micromixing is at least one-order of magnitude faster than the oxygen uptake. Consequently, we do not need to take into account a subgrid-scale model for the interaction of micromixing and reactions and can calculate the reaction rate from the filtered concentration distribution.

In the following, our simulations are compared with results for a well-mixed bulk phase. A simple mass balance gives the differential equation for the well-mixed reactor

$$\varepsilon_L \cdot V_{tot} \cdot \frac{dY_{O_2,mean}}{dt} = k_L \cdot A \cdot (Y_{O_2,I} - Y_{O_2,mean}) - \varepsilon_L \cdot V_{tot} \cdot r_{O_2} \tag{43}$$

Here A is the total gas-liquid interface, and V_{tot} is the total volume of the multiphase mixture, i.e., the volume of the computational domain. After inserting the kinetic expression Eq. 41, the aforementioned equation can be numerically integrated to give the time profile of $Y_{O2,mean}$. The comparison of the simulated mean concentration in the bubble column and the well-mixed reactor is shown in Figure 20a–c. In these plots we have normalized the resulting mean concentration fields by the interface concentration, i.e., $Y_{O_2,I}$. As can be seen, fundamental differences are caused by the oxygen uptake rate. Specifically, we observe that a fast reaction with a small reaction time constant τ leads to a high frequency in the oscillations of the mean concentration. In

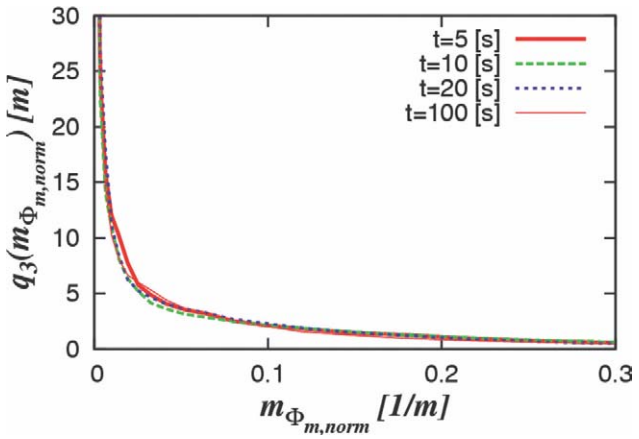

Figure 21. Normalized distribution of the scale of segregation for a reactive scalar (τ_R = 100 s).

[Color figure can be viewed in the online issue, which is available at wileyonlinelibrary.com.]

addition to the high-frequency oscillation in Figure 20a, also a low-frequency oscillation can be observed. This slow change in the mean concentration is caused by the change of the gas holdup, and, consequently, of the interfacial area in the bubble column (refer to the discussion earlier in this article and the curve for $d_p = 1.6$ mm in Figure 16c, where we have quantified the oscillation of the interfacial area a). For slower reaction rates, this low-frequency oscillation is even more pronounced and clearly visibly from Figure 20b and c.

We included two snapshots of the oxygen concentration distribution, as well as the position of individual bubbles in Figure 20e (at t = 52 s, i.e., where the mean concentration in Figure 20b has a local minimum), and Figure 20f (at t = 70 s, i.e., where the mean concentration in Figure 20b has a local maximum). Clearly, the concentration distribution is strongly inhomogeneous in both figures and zones with nearly no oxygen exist. Thus, for these system parameters mass transfer is limiting which leads to regions starving of oxygen.

To quantify mixing under these circumstances, we have plotted the time profiles of the mixing metrics σ^2 and Φ in Figure 20d. This mixing metrics correspond to the time profile of the mean concentration in Figure 20b. Also, we have made the mixing metrics dimensionless by dividing Φ and σ^2 with $Y_{O_2,I}$ and $Y_{O_2,I}{}^2$, respectively. Clearly, both the normalized intensity of segregation σ^2, as well as the normalized scale of segregation Φ, are significantly smaller compared to the case of nonreactive mixing (see Figure 12). Also, the fluctuation of σ^2 is much smaller compared to the case of inert mixing. The scale of segregation Φ is essentially constant indicating a constant mean driving force for mixing. Finally, we have analyzed the distribution of the normalized scale of segregation Φ for the case with a reaction time constant of $\tau_R = 100$ s in Figure 21 for different times. In contrast to the case without reactions, the distribution has a peak at $\Phi = 0$. This is due to the fact, that most of the liquid phase is depleted of dissolved oxygen, and, hence, has zero driving force for mixing. Also, the distribution essentially does not change between the time steps that have been studied, indicating that mixing and the chemical reaction are balanced in this system within a very short time period.

Summary and Conclusion

In this work we have demonstrated that the EL approach together with a large eddy simulation (LES) of the liquid phase is an accurate method to study flow and mixing in dilute bubble swarms. For the first time, we have analyzed in detail:

- the effect of different subgrid-scale models and grid resolution on flow and mixing in dilute bubble swarms,
- new concepts for the quantification of mixing in multiphase systems,
- the distribution of the scale of segregation in multiphase systems,
- the effect of bubble size and gas-flow rate on mixing,
- the effect of scale-up on mixing in dilute bubble swarms, and finally
- the effect of biochemical reactions on different mixing metrics in multiphase systems.

We have shown that the Smagorinsky model with appropriate model constants is able to capture well the mean flow field in the bubble column. More sophisticated differential models, such as the one-equation model used in this work, do not improve accuracy. Furthermore, we have shown that when sophisticated mapping schemes are used, the spurious oscillations, that inevitably occur when using the EL approach, can be suppressed to a large extent. In addition, when using a smart scheme for checking the distance between the particles and the cells, significant computational time can be saved. Also, we have used a novel technique to ensure the conservation of the liquid-phase volume on a fixed grid that does not introduce instabilities as previously reported by other researchers.

Our rigorous investigations have shown that the scale of segregation Φ, the driving force for mixing, is an appropriate metric to interpret mixing involving mass transfer. For example, we have shown that the dimensionless quantity Φ/a, i.e., the scale of segregation normalized with the specific interfacial area, is constant for a certain gas-feed rate but varies with the bubble diameter. Using this dimensionless quantity, the principal mode of mixing, i.e., whether the driving force increases or decreases, can be quantified. We conclude that Φ is uniquely correlated with the bubble diameter, and, consequently, with the specific interfacial area for a given power input, i.e., gas-feed rate. Also, the dimensionless quantity Φ/a is largely unaffected by the scale of the system, i.e., Φ/a will be constant at scale-up. The influence of the gas feed rate on Φ is small, such that Φ/a is a function of the gas-feed rate, and, consequently, the power input. Thus, Φ/a seems to be an appropriate measure to quantify the mixing rate in bubble columns. This effect has been demonstrated in this work for the first time. Clearly, when an appropriate correlation for the gas holdup and the specific interfacial area is available, the scale of segregation can be calculated. This can be then done by knowing the correlation between the specific power input and the dimensionless quantity Φ/a.

Furthermore, our analysis shows that Φ is almost perfectly log-normal distributed. Thus, we anticipate that a simple mathematical model may be derived that allows a theoretical justification of this behavior. Also, this simple mathematical model may be subsequently useful for estimating the yield

and selectivity of reaction networks. This may significantly impact the design of multiphase reactors, as one is not forced to perform high-fidelity simulations, but can estimate yield and selectivity from a simple model.

Furthermore, we have shown that the time scale of meso mixing (ranging from 2–10 s) involving mass transfer is significantly smaller than the time scale for mixing of an inert scalar already dissolved in the liquid phase (ca. 30 s). This is due to the fact that the dissolving gas is already distributed to some extent due to the irregular motion of the individual bubbles. It is clear that the exact relation between these two mixing time scales depends on the geometrical setup of the bubble column. However, it is expected that mixing time scales involving mass transfer are always smaller than time scales without mass transfer for most industrial applications.

Finally, we have investigated how mixing interacts with a liquid-phase chemical reaction, i.e., oxygen uptake by microorganisms. For dilute bubble swarms we could show that the assumption of a well-mixed bulk phase gives reasonable agreement with our detailed numerical predictions. The major part of the deviation between the detailed simulation and the assumed well-mixed bulk phase is due to the fluctuating gas holdup in the simulation. Hence, we conclude that a detailed treatment of liquid-phase reactions requires information on the gas holdup and its fluctuation. Furthermore, the levels of the normalized values for σ^2 and Φ are significantly smaller for a reactive scalar than for a nonreactive one. Also, the principal shape of the distribution of Φ changes from a log-normal (in case of an inert scalar) to a monotonically decreasing function. The predictions for the distribution of the mixing quantities presented in this work may be useful for the construction of a simple mathematical model that is able to predict yield and selectivity in reactive multiphase systems.

Last, we want to conclude that the method presented is also (in principle) capable of describing dense bubble swarms. This is due to the fact that we already take the gas holdup into account when calculating the liquid-phase conservation equations. Sophisticated coalescence, breakage and bubble-bubble interaction models will be incorporated to study also dense bubble swarms in the near future using our method.

Acknowledgments

The authors wish to acknowledge the support of the Austrian Science Foundation through Grant P19639. J. G. Khinast acknowledges partial funding of this work through the EU Marie Curie Chair MEXC-CT-2004-006767.

Notation

a_P^u, a_N^u = coefficients in the system of algebraic equations
A_{cross} = cross-sectional area of the particle, m^2
$A_{\text{p,z}}$ = interfacial area of particle z, m^2
C_A = added mass coefficient
C_e = model constant for the Smagorinsky model
C_ε = model constant for the dynamic subgrid-scale model
C_k = model constant for the Smagorinsky model
C_{L} = lift coefficient
C_s = Smagorinsky constant
d_s = sparger diameter, m
D_i = molecular diffusion coefficient for species i, m^2/s
$D_{\text{eff},i}$ = effective diffusion coefficient for species i, m^2/s
d_p = particle diameter, m
e_{kj} = enumerator reaction exponent of species k in reaction j
E_{kj} = denominator reaction exponent of species k in reaction j
$\mathbf{F}_{\text{A}}$ = added-mass force, kgm/s^2
$\mathbf{F}_{\text{D}}$ = drag force, kgm/s^2
$\mathbf{F}_{\text{G}}$ = gravity force, kgm/s^2
$\mathbf{F}_{\text{L}}$ = lift force, kgm/s^2
$\mathbf{F}_{\text{p}}$ = force due to a pressure gradient, kgm/s^2
$\boldsymbol{g}$ = gravitational acceleration vector, m/s^2
H = height of the bubble column, m
$\boldsymbol{H}(\overline{\mathbf{U}}_{\text{L}})$ = operator involving the known part in the system of algebraic equations
$\boldsymbol{I}$ = identity matrix
k = subgrid-scale kinetic energy, m^2/s^2
k_j = reaction rate constant reaction j (units depending on e_{kj} and E_{kj})
$k_{\text{L}}\cdot a$ = volumetric mass-transfer coefficient, 1/s
$k_{0,0}$ = zero-order reaction rate, $kg/m^3/s$
K_{kj} = reaction constant for species k in reaction j (units depending on E_{kj})
K_{O} = Michaelis-Menten constant in kg/m^3
m_p = particle mass, kg
m_Φ = local distribution of the scale of segregation, 1/m
$m_{\sigma 2}$ = local distribution of the intensity of segregation
$\dot{N}_i$ = mass transfer from the disperse phase, kg/s
$\overline{p}$ = resolved pressure, $kg/m/s^2$
$\overline{p}^*$ = modified pressure (excluding the hydrostatic pressure), $kg/m/s^2$
$\overline{p}'$ = modified kinematic pressure (excluding the hydrostatic pressure), m^2/s^2
Q_3 = cummulative volume distribution of a quantity
q_3 = volumetric frequency distribution of a quantity
$\boldsymbol{r}$ = known part in the system of algebraic equations
r_{O_2} = oxygen uptake rate, $kg/m^3/s$
Re_p = particle Reynolds number
$\bar{S}$ = filtered strain rate tensor, 1/s
Sc_i = Schmidt number of species in the liquid phase
Sc_{SGS} = subgrid-scale Schmidt number
$Sh_{i,z}$ = Sherwood number of species i and particle z
T = thickness of the bubble column, m
$\bar{\boldsymbol{u}}$ = filtered liquid-phase velocity, m/s
$\boldsymbol{u}_{\text{mean}}$ = time-averaged liquid-phase velocity, m/s
$\mathbf{U}$ = particle velocity, m/s
$\mathbf{U}_{\text{rel}}$ = particle relative velocity, m/s
V = volume, m^3
V_G = gas-flow rate, m^3/s
V_{tot} = total reactor volume, m^3
V_p = particle volume, m^3
W = width of the bubble column, m
$x_{\text{cell,max}}$ = maximum distance from the cell center to a cell's boundary point, m
x_{dist} = distance between the cell center and particle, m
x_s = distance of the sparger's center to the left wall of the bubble column, m
$\overline{\text{Y}}_{\text{amp},i,z}$ = ambient concentration of species i near particle z, kg/m^3
$Y_{\text{eq,I}}$ = equilibrium concentration of species i, kg/m^3
$\bar{Y}_i$ = filtered concentration of species i, kg/m_{L}^3
Y_{O_2} = concentration of oxygen in the reactor, kg/m^3
$Y_{\text{O}_2,\text{I}}$ = interface concentration of oxygen in the reactor, kg/m^3
$Y_{\text{O}_2,\text{sat}}$ = oxygen saturation concentration, kg/m^3

Greek letters

β_z = mass-transfer coefficient of particle z, m/s
Δ = filter length, m
ε = subgrid-scale energy dissipation rate, m^2/s^3
ε_{L} = liquid-phase volume fraction, $m^3_{\text{L}}/m^3_{\text{tot}}$
ε_G = gas-phase volume fraction, $m^3_{\text{G}}/m^3_{\text{tot}}$
$\varepsilon_{\text{L,mean}}$ = mean liquid-phase volume fraction, $m^3_{\text{L}}/m^3{}_{\text{tot}}$
$\overline{\varphi}_{\mathbf{L}}$ = filtered liquid phase mass flux, $kg/m^2/s$
Φ = volume-specific coupling force, $kg/m^2/s^2$
Φ = scale of segregation, 1/m
$\Phi_{\dot{N}_i}$ = volumetric source term for species i, $kg/m^3/s$
γ_ρ = density ratio

μ = mean of a distribution
μ_L = dynamic liquid-phase viscosity, Pa.s
$\mu_{eff,L}$ = effective dynamic liquid-phase viscosity, Pa.s
$\mu_{SGS,L}$ = subgrid-scale liquid-phase viscosity, Pa.s
ν = kinematic liquid-phase viscosity, m^2/s
$\nu_{eff,L}$ = effective kinematic liquid-phase viscosity, m^2/s
ρ_L = liquid-phase density, kg/m^3
σ^2 = intensity of segregation
σ = standard deviation of a distribution
$\bar{\tau}_L$ = liquid-phase stress tensor, $kg/m/s^2$
τ_M = micromixing time scale, s
τ_R = reaction time constant, s
ω = rotation vector of the liquid-phase velocity field, 1/s

Literature Cited

1. Troshko AA, Zdravistch F. CFD modeling of slurry bubble column reactors for Fisher-Tropsch synthesis. *Chem Eng Sci*. 2009;64:892–903.
2. Downing RS, Kunkeler PJ, vanBekkum H. Catalytic syntheses of aromatic amines. *Catal Today*. 1997;37:121–136.
3. Mills PL, Chaudhari RV. Reaction engineering of emerging oxidation processes. *Catal Today*. 1999;48:17–29.
4. Tang SW, Liang B. Kinetics of the liquid-phase oxidation of toluene by air. *Ind Eng Chem Res*. 2007;46:6442–6448.
5. Amanullah A, Buckland BC, Nienow AW. *Mixing in the Fermentation and Cell Culture Industries*. In: Paul EL, Atiemo-Obeng VA, Kresta SM. *Handbook of Industrial Mixing - Science and Practice*. Hoboken: John Wiley & Sons, Inc; 2004.
6. Bröder D. *Anwendung optischer Messtechniken zur Untersuchung disperser Gas-Flüssigkeits-Strömungen*. Halle(Saale), Germany: Universität Halle-Wittenberg; 2003.
7. Bork O, Schlueter M, Raebiger N. The impact of local phenomena on mass transfer in gas-liquid systems. *Can J Chem Eng*. 2005;83:658–666.
8. Dani A, Guiraud P, Cockx A. Local measurement of oxygen transfer around a single bubble by planar laser-induced fluorescence. *Chem Eng Sci*. 2007;62:7245–7252.
9. Roy S, Duke SR. Laser induced fluorescence measurements of dissolved oxygen concentration fields near air bubble surfaces. *Rev Sci Instrum*. 2000;71:3494–3501.
10. Roy S, Duke SR. Visualization of oxygen concentration fields and measurement of concentration gradients at bubble surfaces in surfactant-contaminated water. *Exp Fluids*. 2004;36:654–662.
11. Wiemann D, Mewes D. Prediction of backmixing and mass transfer in bubble columns using a multifluid model. *Ind Eng Chem Res*. 2005;44:4959–4967.
12. Yang YB, Devanathan N, Dudukovic MP. Liquid backmixing in bubble-columns. *Chem Eng Sci*. 1992;47:2859–2864.
13. Lorenz O, Schumpe A, Ekambara K, Joshi JB. Liquid phase axial mixing in bubble columns operated at high pressures. *Chem Eng Sci*. 2005;60:3573–3586.
14. Yang NS, Chen BH, Mcmillan AF. Axial mixing and mass-transfer in gas-liquid karr columns. *Ind Eng Chem Proc Design Dev*. 1986; 25:776–780.
15. Sundaresan S. Modeling the hydrodynamics of multiphase flow reactors: Current status and challenges. *AIChE J*. 2000;46:1102–1105.
16. Koynov AA, Khinast JG. Micromixing in reactive, deformable bubble, and droplet swarms. *Chem Eng Technol*. 2006;29:13–23.
17. Sommerfeld M, Decker S. State of the art and future trends in CFD simulation of stirred vessel hydrodynamics. *Chem Eng Technol*. 2004;27:215–224.
18. Kim MS, Lee WI. A new VOF-based numerical scheme for the simulation of fluid flow with free surface. Part I: New free surface-tracking algorithm and its verification. *Int J Numer Methods Fluids*. 2003;42:765–790.
19. Li J, Hesse M, Ziegler J, Woods AW. An arbitrary Lagrangian Eulerian method for moving-boundary problems and its application to jumping over water. *J Comput Phys*. 2005;208:289–314.
20. Hameed M, Siegel M, Young YN, Li J, Booty MR, Papageorgiou DT. Influence of insoluble surfactant on the deformation and breakup of a bubble or thread in a viscous fluid. *J Fluid Mech*. 2008;594:307–340.
21. Unverdi SO, Tryggvason G. A front-tracking method for viscous, incompressible, multi-fluid flows. *J Comput Phys*. 1992;100:25–37.
22. Koynov A, Khinast JG, Tryggvason G. Mass transfer and chemical reactions in bubble swarms with dynamic interfaces. *AIChE J*. 2005;51:2786–2800.
23. Koynov A, Tryggvason G, Schluter M, Khinast JG. Mass transfer and chemical reactions in reactive deformable bubble swarms. *Appl Phys Lett*. 2006;88:134102.
24. Radl S, Koynov A, Tryggvason G, Khinast JG. DNS-based prediction of the selectivity of fast multiphase reactions: hydrogenation of nitroarenes. *Chem Eng Sci*. 2008;63:3279–3291.
25. Radl S, Khinast JG. Prediction of mass transfer coefficients in non-Newtonian fermentation media using first-principles methods. *Biotechnol Bioeng*. 2007;97:1329–1334.
26. Radl S, Tryggvason G, Khinast JG. Flow and mass transfer of fully resolved bubbles in non-Newtonian fluids. *AIChE J*. 2007;53:1861–1878.
27. Darmana D. *On the multiscale modelling of hydrodynamics, mass transfer and chemical reactions in bubble columns*. Twente, Netherlands: University of Twente; 2006.
28. Göz M, Bunner B, Sommerfeld M, Tryggvason G. Direct numerical simulation of bidisperse bubble swarms. International Conference on Multiphase Flow; 2001; New Orleans, LA.
29. Göz M, Bunner B, Sommerfeld M, Tryggvason G. Direct numerical simulation of bubble swarms with a parallel front-tracking method. International FORTWIHR Conference on HPSEC; 2001; Erlangen, Germany.
30. Raffensberger JA, Glasser BJ, Khinast JG. Analysis of heterogeneously catalyzed reactions close to bubbles. *AIChE J*. 2005;51:1482–1496.
31. Lehr F, Millies M, Mewes D. Bubble-size distributions and flow fields in bubble columns. *AIChE J*. 2002;48:2426–2443.
32. Delnoij E, Lammers FA, Kuipers JAM, vanSwaaij WPM. Dynamic simulation of dispersed gas-liquid two-phase flow using a discrete bubble model. *Chem Eng Sci*. 1997;52:1429–1458.
33. Crowe C, Sommerfeld M, Tsuji Y. *Multiphase Flows with Droplets and Particles*. Boca Raton: CRC Press; 1998.
34. Sommerfeld M. *Modellierung und numerische Berechnung von partikelbeladenen turbulenten Strömungen mit Hilfe des Euler/Lagrange-Verfahrens*. Aachen: Shaker Verlag; 1996.
35. Nierhaus T, Abeele DV, Deconinck H. Direct numerical simulation of bubbly flow in the turbulent boundary layer of a horizontal parallel plate electrochemical reactor. *International J Heat Fluid Flow*. 2007;28:542–551.
36. Deen NG, Solberg T, Hjertager BH. Large eddy simulation of the gas-liquid flow in a square cross-sectioned bubble column. *Chem Eng Sci*. 2001;56:6341–6349.
37. Tomiyama A, Zun I, Higaki H, Makino Y. A three-dimensional particle tracking method for bubbly flow simulation. *Nucl Eng Des*. 1997;175:77–86.
38. Arlov D, Revstedt J, Fuchs L. Numerical simulation of a gas-liquid Rushton stirred reactor - LES and LPT. *Comput Fluids*. 2008;37:793–801.
39. Hu GS, Celik I. Eulerian-Lagrangian based large-eddy simulation of a partially aerated flat bubble column. *Chem Eng Sci*. 2008;63:253–271.
40. Bini M, Jones WP. Particle acceleration in turbulent flows: A class of nonlinear stochastic models for intermittency. *Phys Fluids*. 2007;19:035104.
41. van Dijk GJ. *The implementation of a Lagrangian Particle Dispersion Model in Large Eddy Simulations of the Atmospheric Boundary Layer*. Delft University of Technology, The Netherlands; 2007.
42. Marchioli C, Salvetti MV, Soldati A. Some issues concerning large-eddy simulation of inertial particle dispersion in turbulent bounded flows. *Phys Fluids*. 2008;20:040603.
43. Martin M, Montes FJ, Galan MA. On the contribution of the scales of mixing to the oxygen transfer in stirred tanks. *Chem Eng J*. 2008;145:232–241.
44. Baldyga J, Bourne JR, Walker B. Non-isothermal micromixing in turbulent liquids: Theory and experiment. *Can J Chem Eng*. 1998;76:641–649.
45. Bourne JR, Hilber CP. The productivity of micromixing-controlled reactions - effect of feed distribution in stirred tanks. *Chem Eng Res Des*. 1990;68:51–56.
46. Bourne JR, Kut OM, Lenzner J. An improved reaction system to investigate micromixing in high-intensity mixers. *Ind Eng Chem Res*. 1992;31:949–958.
47. Bourne JR, Yu SY. Investigation of micromixing in stirred-tank reactors using parallel reactions. *Ind Eng Chem Res*. 1994;33:41–55.

48. Paul EL, Treybal RE. Mixing and product distribution for a liquid-phase, second-order, competitive-consecutive reaction. *AIChE J*. 1971;40:718.
49. Lin WW, Lee DJ. Micromixing effects in aerated stirred tank. *Chem Eng Sci*. 1997;52:3837–3842.
50. Fournier MC, Falk L, Villermaux J. A new parallel competing reaction system for assessing micromixing efficiency - Experimental approach. *Chem Eng Sci*. 1996;51:5053–5064.
51. Fournier MC, Falk L, Villermaux J. A new parallel competing reaction system for assessing micromixing efficiency - Determination of micromixing time by a simple mixing model. *Chem Eng Sci*. 1996;51:5187–5192.
52. Luo HP, Al-Dahhan MH. Macromixing in a draft-tube airlift bioreactor. *Chem Eng Sci*. 2008;63:1572–1585.
53. Al-Dahhan MH, Mills PL, Gupta P, Han L, Dudukovic MP, Leib TM et al. Liquid-phase tracer responses in a cold-flow counter-current trayed bubble column from conductivity probe measurements. *Chem Eng Proc*. 2006;45:945–953.
54. Alvare J, Al-Dahhan MH. Liquid phase mixing in trayed bubble column reactors. *Chem Eng Sci*. 2006;61:1819–1835.
55. Moustiri S, Hebrard G, Thakre SS, Roustan M. A unified correlation for predicting liquid axial dispersion coefficient in bubble columns. *Chem Eng Sci*. 2001;56:1041–1047.
56. Vial C, Poncin S, Wild G, Midoux N. Experimental and theoretical analysis of axial dispersion in the liquid phase in external-loop airlift reactors. *Chem Eng Sci*. 2005;60:5945–5954.
57. Joshi JB. Computational flow modelling and design of bubble column reactors. *Chem Eng Sci*. 2001;56:5893–5933.
58. Khinast JG. Impact of 2-D bubble dynamics on the selectivity of fast gas-liquid reactions. *AIChE J*. 2001;47:2304–2319.
59. Derksen JJ. Scalar mixing by granular particles. *AIChE J*. 2008;54:1741–1747.
60. Derksen JJ. Mixing by solid particles. *Chem Eng Res Des*. 2008;86:1363–1368.
61. Roy S, Joshi JB. Effect of liquid velocity on axial mixing in gas-liquid dispersions: A CFD simulation. *Chem Eng Technol*. 2006;29:1034–1041.
62. Joshi JB. Computational flow modelling and design of bubble column reactors. *Chem Eng Sci*. 2001;56:5893–5933.
63. deVilliers E. *The Potential of Large Eddy Simulation for the Modeling of Wall Bounded Flows*. London, U.K: Imperial College of Science, Technology and Medicine; 2006.
64. Sato Y, Sekoguchi K. Liquid velocity distribution in 2-phase bubble flow. *Bull Jsme-Jpn Soc Mech Eng*. 1976;19:825.
65. Niceno B, Dhotre MT, Deen NG. One-equation sub-grid scale (SGS) modelling for Euler-Euler large eddy simulation (EELES) of dispersed bubbly flow. *Chem Eng Sci*. 2008;63:3923–3931.
66. Spalding DB. A single formula for the law of the wall. *J Appl Mech*. 1961;28:455–458.
67. Clift R, Grace JR, Weber ME. *Bubbles, Drops, and Particles*. Mineola, NY: Dover Publications, Inc; 2005.
68. Becker S, Sokolichin A, Eigenberger G. Gas-liquid flow in bubble columns and loop reactors: Part II. Comparison of detailed experiments and flow simulations. *Chem Eng Sci*. 1994;49:5747–5762.
69. Auton TR. *The dynamics of Bubbles, Drops and Particles in Motion in Liquids*. Cambridge, U.K: University of Cambridge; 1983.
70. Loth E. Numerical approaches for motion of dispersed particles, droplets and bubbles. *Prog Energy Combust Sci*. 2000;26:161–223.
71. Mei RW, Lawrence CJ, Adrian RJ. Unsteady drag on a sphere at finite reynolds-number with small fluctuations in the free-stream velocity. *J Fluid Mech*. 1991;233:613–631.
72. Sridhar G, Katz J. Drag and lift forces on microscopic bubbles entrained by a vortex. *Phys Fluids*. 1995;7:389–399.
73. Tominaga Y, Stathopoulos T. Turbulent Schmidt numbers for CFD analysis with various types of flowfield. *Atmos Environ*. 2007;41:8091–8099.
74. Feng W, Wen JP, Liu CY, Yuan Q, Jia XQ, Sun Y. Modeling of local dynamic behavior of phenol degradation in an internal loop airlift bioreactor by yeast candida tropicalis. *Biotechnol Bioeng*. 2007;97:251–264.
75. Fox RO. *Computational Models for Turbulent Reacting Flows*. Cambridge, UK: Cambridge University Press; 2003.
76. Bird RB, Stewart WE, Lightfood EN. *Transport Phenomena*. New York: John Wiley & Sons, Inc; 2002.
77. Marchisio DL. Large Eddy Simulation of mixing and reaction in a confined impinging jets reactor. *Comput Chem Eng*. 2009;33:408–420.
78. Lindenberg C, Scholl J, Vicum L, Mazzotti M, Brozio J. Experimental characterization and multi-scale modeling of mixing in static mixers. *Chem Eng Sci*. 2008;63:4135–4149.
79. OpenFoam 1.5 User Guide (www.opencfd.co.uk). OpenCFD, Ltd., 2008.
80. Jasak H. *Error Analysis and Estimation for the Finite Volume Method with Applications to Fluid Flow*. London, U.K: Department of Mechanical Engineering, Imperial College of Science, Technology and Medicine; 1996.
81. Deen NG, Sint Annaland A, Kuipers JAM. Multi-scale modeling of dispersed gas-liquid two-phase flow. *Chem Eng Sci*. 2004;59:1853–1861.
82. Rusche H. *Computational Fluid Dynamics of Dispersed Two-Phase Flows at High Phase Fractions*. London, U.K: Imperial College of Science, Technology and Medicine; 2002.
83. Issa RI. Solution of the implicitly discretized fluid-flow equations by operator-splitting. *J Comput Phys*. 1986;62:40–65.
84. Nilsson H. CFD with OpenSource Software. Gothenburg, Sweden: Chalmers University of Technology; 2008. PhD. Internet communication.
85. Kaerrholm FP. *Numerical Modelling of Diesel Spray Injection, Turbulence Interaction and Combustion*. Gothenburg, Sweden: Chalmers University of Technology; 2008.
86. MacPherson GB, Nordin N, Weller HG. Particle tracking in unstructured, aritrary polyhedral meshes for use in cfd and molecular dynamics. *Commun Numer Methods Eng*. 2009;25:263–273.
87. Sokolichin A, Eigenberger G. Applicability of the standard k-epsilon turbulence model to the dynamic simulation of bubble columns: Part I. Detailed numerical simulations. *Chem Eng Sci*. 1999;54:2273–2284.
88. Diaz ME, Iranzo A, Cuadra D, Barbero R, Montes FJ, Galan MA. Numerical simulation of the gas-liquid flow in a laboratory scale bubble column Influence of bubble size distribution and non-drag forces. *Chem Eng J*. 2008;139:363–379.
89. Hu GS. *Towards Large Eddy Simulation of Dispersed Gas-Liquid Two-Phase Turbulent Flows*. Morgantown, WV: West Virginia University; 2005.
90. Bothe D, Sternich C, Warnecke HJ. Fluid mixing in a T-shaped micro-mixer. *Chem Eng Sci*. 2006;61:2950–2958.
91. Bothe D, Stemich C, Warnecke HJ. Theoretical and experimental studies on the mixing processes in T-shaped microreactors - Part 1: Numerical simulation and assessment of flow mixing. *Chemie Ingenieur Technik*. 2004;76:1480–1484.
92. Bothe D, Stemich C, Warnecke HJ. Computation of scales and quality of mixing in a T-shaped microreactor. *Comput Chem Eng*. 2008;32:108–114.
93. Celik IB, Cehreli ZN, Yavuz I. Index of resolution quality for large eddy simulations. *J Fluids Eng Trans Asme*. 2005;127:949–958.
94. Sweere APJ, Luyben KCAM, Kossen NWF. Regime analysis and scale-down - tools to investigate the performance of bioreactors. *Enzyme Microb Technol*. 1987;9:386–398.
95. Patterson GK, Paul EL, Kresta SM.*Mixing and Chemical Reactions*. In: Paul EL, Atiemo-Obeng VA, Kresta SM. *Handbook of Industrial Mixing - Science and Practice*. Hoboken: John Wiley & Sons, Inc; 2004:755–868.

Manuscript received May 10, 2009, and revision received Nov. 18, 2009.